Comparison of Jet Quenching Formalisms for a Quark-Gluon Plasma "Brick"

Nestor Armesto,[1] Brian Cole,[2] Charles Gale,[3] William A. Horowitz,[4,6] Peter Jacobs,[7] Sangyong Jeon,[3] Marco van Leeuwen,[8] Abhijit Majumder,[4,5] Berndt Müller,[9] Guang-You Qin,[9] Carlos A. Salgado,[1] Björn Schenke,[3,10] Marta Verweij,[8] Xin-Nian Wang,[11,7] and Urs Achim Wiedemann[12]

[1]*Departamento de Física de Partículas and IGFAE, Universidade de Santiago de Compostela, E-15706 Santiago de Compostela, Spain*
[2]*Columbia University, Physics Department and Nevis Laboratories, PO Box 137, Irvington NY, 10533*
[3]*Department of Physics, McGill University, Montreal QC H3A-2T8, Canada*
[4]*Department of Physics, The Ohio State University, Columbus, OH 43210, USA*
[5]*Department of Physics, Wayne State University, Detroit, MI 48201*
[6]*Department of Physics, University of Cape Town, Private Bag X3, Rondebosch 7701, South Africa*
[7]*Nuclear Science Division, Lawrence Berkeley National Laboratory, Berkeley, CA 94720, USA*
[8]*Nikhef, National Institute for Subatomic Physics and Institute for Subatomic Physics of Utrecht University, Utrecht, Netherlands*
[9]*Department of Physics & CTMS, Duke University, Durham, NC 27708, USA*
[10]*Physics Department, Bldg. 510A, Brookhaven National Laboratory, Upton, NY 11973, USA*
[11]*Institute of Particle Physics, Central China Normal University, Wuhan 430079, China*
[12]*Department of Physics, CERN, Theory Unit, CH-1211 Geneva 23, Switzerland*

(Dated: February 17, 2022)

We review the currently available formalisms for radiative energy loss of a high-momentum parton in a dense strongly interacting medium. The underlying theoretical framework of the four commonly used formalisms is discussed and the differences and commonalities between the formalisms are highlighted. A quantitative comparison of the single gluon emission spectra as well as the energy loss distributions is given for a model system consisting of a uniform medium with a fixed length of $L = 2$ fm and $L = 5$ fm (the 'Brick'). Sizable quantitative differences are found. The largest differences can be attributed to specific approximations that are made in the calculation of the radiation spectrum.

arXiv:1106.1106v2 [hep-ph] 22 Nov 2012

I. INTRODUCTION

QCD jets are produced in hadronic interactions of all kinds, by the hard scattering of the constituent partons (quarks and gluons) of the colliding projectiles. One of the most significant experimental discoveries in the collision of heavy nuclei at $\sqrt{s_{NN}} = 200$ GeV at the Relativistic Heavy Ion Collider (RHIC) was the observation of a strong suppression of the inclusive yield of high momentum (high p_T) hadrons [1, 2] and the semi-inclusive rate of azimuthally back-to-back high p_T hadron pairs relative to expectations from p+p and d+Au collisions [3–5], as expected from jet quenching by the hot and dense medium formed in these collisions. Evidence for jet quenching has also been observed recently in Pb+Pb collisions at the LHC [6–8].

Most generally, the term 'jet quenching' refers to the modification of the evolution of an energetic parton induced by its interactions with a colored medium. The expected manifestations of modified evolution of parton showers include the suppression of hadronic spectra at high p_T and their back-to-back azimuthal correlations, as well as the enhancement of hadron spectra at low p_T and possibly the angular broadening of internal jet structure and di-jet acoplanarity.

Data from the RHIC heavy ion program strongly support the picture that jet quenching is caused by the loss of energy of the primary parton, either by collisions with constituents of the medium (collisional or elastic energy loss [9, 10]) or by gluon bremsstrahlung (radiative or inelastic energy loss [11–13]), prior to hadronization in the vacuum. The loss of energy suffered by an energetic quark or gluon penetrating a QCD medium probes dynamical properties of the medium. Jet quenching provides unique and powerful tools for studying the properties of the hot and dense matter produced in heavy ion collisions.

In recent years, a number of different dynamical models of jet quenching has been formulated and compared to the jet quenching signatures measured at RHIC (see [14–17] for reviews). These models are based on the common assumption that interactions of the energetic parton and the radiated gluon with the medium can be calculated via perturbative QCD (pQCD), regardless whether the properties of the medium itself can be treated perturbatively. Within such perturbative approaches, however, different approximations exist in the calculation of radiative energy loss of the leading parton. Direct comparisons of the various pQCD-based models show large quantitative discrepancies in the medium density that is needed to describe the same suppression of the inclusive production of light leading mesons [18–20]. The full modeling of jet quenching in the complex, dynamic process of heavy ion collisions contains a large number of components, including the initial production spectrum, a time-dependent medium density profile, and fragmentation. The com-

plexity of the modeling, with each model at present employing a different dynamical framework, makes it difficult to isolate the specific differences between the energy loss formalisms, and thereby to constrain the underlying mechanisms of jet quenching through full model comparisons.

In this paper we review the current state of the art of pQCD-based radiative energy loss models, including a discussion of their theoretical foundations and limitations, their kinematic region of applicability, as well as various model-dependent sources of uncertainty. In order to make a direct comparison of the models, we provide a systematic quantitative comparison of energy loss formalisms using a highly simplified model problem: the energy loss of light quarks in a static medium of constant density and a fixed length, known as the QGP brick.We will restrict the discussion to leading parton energy loss, for which the largest body of theoretical work exists.

The paper is organized as follows. The first section provides an executive summary of our main findings, with particular emphasis on common features, technical and conceptual differences, and uncertainties of different jet quenching models. This section is a self-contained narrative with a short introduction to the different classes of jet quenching models. It is intended to be accessible to a non-expert reader. Many of the technical details will be omitted from the executive summary, which refers to following sections for more detailed explanations and numerical studies supporting the main statements. For more extensive descriptions of the various jet quenching formalisms and of the available phenomenology including model–data comparisons, we refer to the existing reviews [14–17]

II. EXECUTIVE SUMMARY

A. Jet quenching is caused by partonic interactions in dense matter

We first discuss the factorized perturbative QCD framework for calculating jet and hadron production in the absence of medium effects. In elementary collisions (e^+e^-, pp, and $\bar{\text{p}}$p), our understanding of hadron production at high transverse momentum is relatively mature. High-p_T hadron production results from partonic processes with large momentum transfer that can be described with controlled uncertainty as the convolution of incoming parton distribution functions (PDFs), a hard partonic collision process, and the fragmentation of the partonic final state [21]. The PDFs and Fragmentation Functions (FFs) are universal, non-perturbative, scale-dependent distributions that obey DGLAP evolution and are determined by global fits to data from elementary collisions [22–26].

In ultra-relativistic heavy ion collisions, there is currently no firm theoretical argument that production cross sections factorize. Rather, factorization is a working assumption that is consistent with phenomenological analyses made so far and that underlies all models discussed in this report. General considerations indicate that if factorization is assumed, the hard partonic interaction itself cannot be modified by the medium, since it occurs on temporal and spatial scales too short to be resolved by the medium. However, it is also expected on general grounds that the parton distribution functions in nuclei differ from those in nucleons, and it is possible that the fragmentation of outgoing partons is modified by the presence of a hot QCD medium.

We know with certainty that jet quenching receives its main contribution on the level of the outgoing fragmenting parton. This follows from several lines of argument. In particular, it is found that the production of direct photons, which have no strong interaction with medium, does not show the large suppressions characteristic for jet quenching [27]. Moreover, there are by now several global PDF fits that parametrize the nuclear dependence of incoming parton distribution functions (nPDFs). For the typical momentum fractions x and virtualities Q relevant for hard processes, these nPDF-fits show nuclear modifications of the order of 10-30 % that cannot account for the observed factor 4-5 suppression of single inclusive hadron spectra [28, 29]. Therefore, the energy degradation observed in nucleus-nucleus collision for all hadronic high transverse momentum spectra must be due to dynamical effects occurring after the hard process ('final state effects').

Furthermore, there is strong experimental evidence that the final state effect responsible for jet quenching is of partonic nature, i.e., that it occurs prior to hadronization. In particular, correlations of high p_T hadron pairs with small angular separation are largely unmodified in systems that exhibit strong inclusive suppression [3–5]. In addition, there is no evidence that the characteristically different nuclear 'absorption' cross sections of different hadron species play a role in understanding the jet quenching effect.

As a consequence of these generic observations, all current efforts to understand and simulate jet quenching are based on models of parton energy loss. Further progress then depends on promoting the relation between jet quenching phenomenology and parton energy loss from a qualitative to a more and more quantitative one. To this end, we embark in the following on a critical assessment of current parton energy loss models.

B. Models of radiative parton energy loss

The elementary branching process within a medium of finite size L is depicted in Fig. 1. Calculations of radiative parton energy loss aim at determining such processes within the framework of perturbative QCD. All approaches studied so far involve significant assumptions and approximations about

- the virtuality and (repeated) branching of the hard

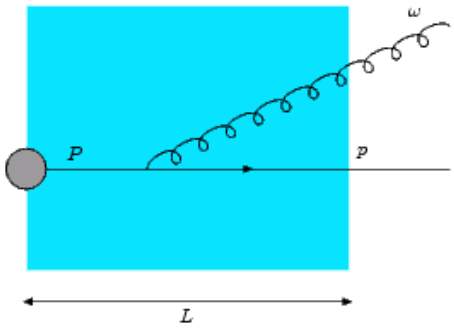


FIG. 1: Schematic view of a hard parton-parton interactions (grey blob) producing a highly energetic parton, which subsequently undergoes parton branching processes. In a heavy ion collision, this parton evolution occurs within a dense medium (blue area) that interferes with the vacuum evolution via *a priori* unknown elastic and inelastic interactions.

parton;

- the nature of the medium through which the energetic parton propagates; and
- kinematical approximations for the interaction between medium and projectile parton.

It will turn out that the largest quantitative differences among the various models arise not so much from differences in their basic underlying assumptions about the medium and its interaction with the high energy parton, but rather in the implementation of the simplifying approximations made to carry out the derivations and calculations, most importantly, the treatment of energy-momentum constraints and large angle radiation.

In the remainder of this Section, we will first provide a short general discussion of in-medium QCD radiation, before describing the specific implementations.

1. *Virtuality and parton branching in the medium*

A high-p_T parton, produced by a hard initial collision between incoming partons, carries initially a high virtuality. Even in the absence of a medium, the parton will undergo 'vacuum' splitting processes to reduce its off-shellness. When the radiations occurs in the medium, the question arises whether this parton splitting is just the same as in the vacuum, or rather an additional medium-induced splitting, or a result of the interference between medium-induced effects and dynamics that would also occur in the absence of a medium. None of the existing parton energy loss calculations treats the entire dynamics depicted in Fig. 1 in a field-theoretically rigorous fashion.

The medium effect on parton splitting is brought about by interactions of the high-energy parton and the radiated gluon with the medium. For small-angle scattering, the parton and the radiated gluon propagate along similar paths, leading to significant interference and a finite formation time of the gluon, which suppresses the gluon radiation compared to incoherent emission. This effect is often referred to as the Landau-Pomeranchuk-Migdal effect. A characteristic consequence of this interference is that the amount of energy loss grows quadratically with L for in-medium path lengths that are small compared to the formation time [12].

In general, multiple splittings may occur in the medium. A full calculation of multi-gluon final states would include interference terms between the different emitted gluons. Recently some progress has been made on this particular problem, using calculations of the interference between two emitters (the antenna problem), which show interesting features as angular ordering or partial decoherence [30–33]. The generalization of these results to multiple gluon emission is not known at present and all current calculations are based on repeated application of a single-gluon emission calculation. In the following we will separately discuss the single-gluon radiation kernel and the prescription used for multiple gluon emission.

2. *Modeling the medium*

The main interest in studying jet quenching is to use it to characterize the medium through which the projectile parton propagates. It is of great interest to implement different models of the medium in jet quenching calculations to determine how the medium model and properties affect jet quenching. In the current practice, each model description uses a particular set of simplifications, which can be classified as follows:

1. *The medium is modeled as a collection of static scattering centers*
   In this approach, the medium is modeled as a set of static colored scattering centers with a specified density distribution along the trajectory of the projectile. A decreasing density approximates the effects of an expanding medium. Because gluon radiation from the scattering centers is ignored, calculations in this set-up lead to gauge-invariant (i.e. physically meaningful) results only to leading order in a high-energy approximation. By construction this set-up neglects recoil effects and thus does not allow for elastic parton energy loss.

   This medium model was pioneered by Baier, Dokshitzer, Mueller, Peigné and Schiff [12, 34, 35] (BDMPS) and independently by Zakharov [36, 37]. Gluon radiation is formulated in a path-integral that resums scatterings on multiple static colored scattering centers. Wiedemann [38] showed how this path-integral can be used to include interference effects between vacuum and medium-induced radiation in such a way that also the $k_\perp$-differential

medium-induced gluon distribution is accounted for.

In the original BDMPS derivation of the medium-induced gluon distribution [12, 34], the soft gluon approximation, $x \ll 1$, was used. In later derivations [35], the radiation spectrum is multiplied by an overall splitting function to take corrections for finite x into account. In the literature, the term "BDMPS-Z formalism" has been used for both versions of the formalism. The difference between the radiation spectrum with and without this splitting function $P_{s\to g}(x)$ is discussed in Section III C 5 and Fig. 14.

Most analytical and numerical results from the BDMPS–Z formalism use a saddle point approximation that amounts effectively to assuming that the projectile interacts with the medium via *multiple soft scattering* processes. In the following, the numerical results from the low-x, multiple soft scattering implementation of the BDMPS–Z formalism are based on the work by Armesto, Salgado and Wiedemann [38–40], abbreviated as ASW–MS. In the totally coherent limit, in which the entire medium acts coherently towards gluon production, the multiple-soft scattering formalism results in a radiation spectrum that is a radiation term for gluon production with momentum transfer $\mathbf{q}_\perp$ convoluted with a Gaussian elastic scattering cross section $\propto \frac{1}{\hat{q}\,L}\exp\left[-\mathbf{q}_\perp^2/\hat{q}\,L\right]$. In this limit, the medium is fully characterized by the transport coefficient $\hat{q}$, the mean of the squared transverse momentum exchanged per unit path length.

The *opacity expansion* was pioneered by Gyulassy, Levai and Vitev [41, 42] (GLV) and independently by Wiedemann [38]. It also includes the interference between vacuum and medium-induced radiation and is based on a systematic expansion of the calculation in terms of the number of scatterings. Since the BDMPS–Z path-integral formalism can serve as a generating functional for the opacity expansion [38], the opacity expansion formalism is another limit for the solution of the BDMPS–Z path integral.

In most existing calculations, only the leading term ($N = 1$) is included, but the behaviour for larger opacities has been explored in [43, 44]. The medium is characterized by two model parameters, the density of scattering centers n or mean free path λ, and a Debye screening mass μ_D used to regulate the infrared behavior of the single scattering cross section. In contrast to the multiple soft scattering approximation, this approach includes the power-law tail of the scattering cross section expected from QCD, leading to shorter formation times of the radiation compared to the multiple-soft scattering approximation [45]. There are several model implementations in the literature that differ significantly in their kinematic approximations. We will use two implementations (ASW-SH and DGLV [46, 47]) to discuss the differences in detail in Section III B. Extension of the opacity expansion formalism to a medium with dynamical scattering centers was recently explored by Djordjevic and Heinz [48].

2. *The medium is characterized by matrix elements of gauge field operators*
   In principle, multiple gluon exchanges between a partonic projectile and a spatially extended medium can be formulated in a field theoretically rigorous fashion by describing the medium in terms of expectation values of 2-, 4-, 6-, 8-, ... field correlation functions. Energy loss calculations based on the higher-twist (HT) approach were pioneered by Guo and Wang [49, 50]. The approach includes the interference between vacuum and medium-induced radiation. Properties of the medium enter the calculation in terms of higher-twist matrix elements. In practice the matrix elements are factorized in the nPDF and matrix elements describing the interaction between final state partons and the medium. This factorization is valid at leading order in the path length L in the medium. As we discuss in some detail in Section III D, the approximations currently employed result in a formulation of parton energy loss calculations that closely resembles models starting from a set of static scattering centers.

3. *Thermally equilibrated, perturbative medium*
   The formulation in rigorous field-theory of parton energy loss in a weakly-coupled medium in perfect thermal equilibrium was developed by Arnold, Moore and Yaffe [51, 52] (AMY). The medium is formulated as a thermal equilibrium state in Hard Thermal Loop improved finite temperature perturbation theory. As a consequence, all properties of the medium are specified fully by its temperature and baryon chemical potential. The calculation does not incorporate vacuum branching of the projectile parton. In principle, the perturbative description of the thermal medium applies only at very high temperature $T \gg T_c$.

As seen from the list above, different models of parton energy loss characterize the medium in terms of different primary model parameters. In the existing literature, the different approximations used for the medium in the various approaches have led to different ways to specify the medium properties. Recently it has become customary to translate the primary model parameters into an effective $\hat{q}$, that has the physical interpretation of an averaged squared momentum transfer between the medium and the fast parton per unit path length $\hat{q} = \langle q_\perp^2\rangle/\lambda$. This transport coefficient can be calculated from the differential scattering cross section $d\sigma/d^2q_\perp$ in the medium or the rate of momentum exchange, $d\Gamma_{el}/d^2q_\perp$. In this

paper, we will use a common approach to calculate $\hat{q}$, using rates from Hard Thermal Loop (HTL) effective field theory. The basic parameters in the opacity expansion are the screening length μ_D and the mean free path λ, which can also be calculated in HTL. For details, we refer the reader to Appendix A.

3. Kinematic approximations in different parton energy loss models

With regard to the technical approximations employed in parton energy loss calculations, the four model classes show important commonalities, but also display characteristic differences.

The three main assumptions that are made in all the calculations are:

- Both the parton and the radiated gluon are on eikonal trajectories: the parton energy E is much larger than the transverse momentum exchanged with the medium $q_\perp$, $E \gg q_\perp$ and the energy of the emitted gluon ω is also much larger than the exchanged momentum: $\omega \gg q_\perp$.
- Small-angle (collinear) radiation: the energy of the gluon is much larger than its transverse momentum k_T, $\omega \gg k_T$
- Discrete scattering centers, or some form of localised momentum transfer: the mean free path λ is much larger than the Debye screening length $1/\mu$ $\lambda \gg 1/\mu$.

Since the eikonal approximation is used, one often uses the additional approximation that the gluon energy is much smaller than the parton energy $\omega \ll E$, or $x = \omega/E \ll 1$, i.e. the soft radiation approximation. This approximation is not made in the AMY calculation.

Let us first consider the kinematic constraints $E \gg \omega \gg k_T, q_\perp$, which is often referred to as the soft eikonal limit. In the calculations, this limit is used for example to neglect the changes to the parent trajectory due to multiple scattering, which simplifies the calculations significantly. In phenomenological applications of parton energy loss, however, gluon radiation is calculated in the entire allowed phase space, up to $\omega = E$ and $k_T = \omega$, where the approximations are not valid. The approximations employed in the current calculations lead to finite radiation probability at the kinematic bounds $\omega \approx E$ and $k_T \approx \omega$, thus violating energy-momentum conservation. Most current formalisms remedy this by imposing explicit cut-offs at the kinematic bounds. The sensitivity of the result to large-x and large angle radiation can be explored to get an impression of the accuracy of the result. The two limits warrant separate discussions.

Consider the large-x regime, where $\omega \approx E$. For all energy loss models, the gluon energy distribution peaks at a "typical" energy (which may be very small). As a result, one can always restrict the considerations (and in most cases the measurement as well) to a reasonably high parton energy for which the calculated rate at $x \to 1$ is small compared to the total rate, thus giving confidence that the impact of the cut-off at $x = 1$ is small. For typical medium densities at RHIC, the gluon energy ω peaks at $O(1$ GeV), so that for parton energies $E \gtrsim 10$ GeV, the probability density at the kinematic boundary becomes reasonably small.

In the present calculational framework, the yield in the spectrum for $\omega > E$, i.e. above the kinematical boundary can be taken as a probability of total absorption of the parton, 'death before arrival'. We note that simply ignoring the radiation spectrum beyond the kinematic limit leads to the unphysical result that in some cases the total radiation probability decreases with increasing density or path length, when the typical gluon energy is close to E. In the AMY formalism, $\omega > E$ is kinematically allowed because interactions with dynamic medium allow the propagating parton to absorb energy from the medium when E is not much larger than T, which is then re-emitted.

The situation is different for large-angle radiation. In the presently existing formalisms, the typical transverse momentum of the radiated gluon k_T depends on the typical transverse momentum exchanges $q_\perp$ and the number of scatterings L/λ, but not on the gluon energy ω. As a result, there is always some radiation with ω smaller than the typical k_T and thus with a large probability for radiation at $k_T \to \omega$. The quantitative impact of large angle radiation depends on the medium model (large $q_\perp$ contributions in the medium cross section) and the choice of parameters. Already in an early publication it was pointed out that the large-angle regime may be important for phenomenological applications, for example in [53]: " ... the BDMPS–Z formalism is based on the assumption of small transverse gluon momentum $|k_T| \ll \omega$ while we find the main contribution to radiative energy loss for $|k_T| = O(\omega)$. Both features question the validity of the BDMPS–Z formalism ..." A detailed discussion of the effect of large angle radiation in the opacity expansion framework in given in Section III B and in [54].

4. Multiple gluon emission

Multiple gluon emission is calculated by repeating the single gluon emission kernel as needed.

The simplest procedure for multiple gluon emission is the Poisson ansatz, where the number of emitted gluons follows a Poisson distribution, with the mean number given by the integral of the gluon emission spectrum. The energy distribution of each gluon follows the single gluon emission kernel. This procedure is used by GLV and ASW. In most cases relevant to the experimental conditions at RHIC, the mean number of radiated gluons $\langle N_g \rangle > 1$, so that the mean total energy loss $\langle \Delta E \rangle$ is larger than the mean of the energy of a single gluon $\langle \omega \rangle$. In general, this procedure leads to a distribution of lost

energy that does not conserve energy as the degrading momentum of the parent parton is not dynamically updated. However, in most cases, the probability to radiate a larger energy than the incoming parton energy is limited, so that the uncertainty associated with this effect is small. For a more detailed study, see [55]. Interference effects between medium-induced radiation and vacuum radiation are included in the single-gluon emission spectra, but the parton is assumed to fragment in the vacuum after energy loss.

HT and AMY both use a coupled evolution procedure to calculate multiple gluon emission. In the case of HT, medium-modified DGLAP evolution is used, which includes the virtuality evolution in vacuum. In the AMY approach, rate equations are used and no vacuum radiation is included. However, recent work [56] has addressed this issue and showed how it can be included in the same framework.

The evolution equations used in HT and AMY both include the coupling between the quark and gluon distributions in the jets and keep track of the gradual degradation of the jet energy. The emission probability distribution changes as the jet energy degrades, which is in principle a significant conceptual improvement over the Poisson convolution approach. There is, however, an important point that is not explicitly addressed in any of the models: as the energy degrades, the remaining path length through the medium also decreases. So, in principle, the energy-evolution should be accompanied by an evolution in coordinate space and the emission probabilities should be calculated using local information about the parton energy, the medium, and the remaining path length. Some models do take into account the evolution of the medium and corresponding change in the local environment of the propagating parton. However, combining both local information and the true finite size effect proves to be a difficult problem in the presence of interference effects, where the gluon radiation is not a purely local phenomenon, but instead couples to the parton over an extended area.

C. Schemes of radiative parton energy loss

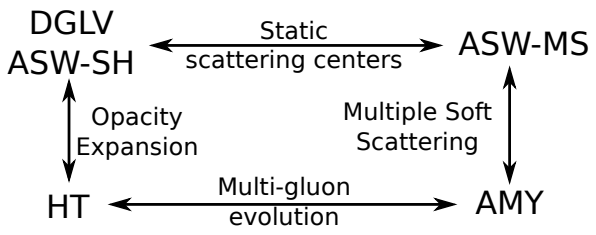


FIG. 2: The landscape of pQCD based jet quenching formalisms. Arrows indicate common concepts or assumptions between adjacent formalisms.

In the previous sections, we outlined both the single-gluon emission calculations as well as the multiple gluon calculations that are commonly used in the literature. To gain a better understanding of the various formalisms, it is useful to compare and contrast closely related formalisms. Fig. 2 illustrates the close technical and conceptual relations between the different models of parton energy loss.

1. *Multiple soft scattering vs Opacity expansion*
   The multiple soft scattering approximation and the opacity expansion can be shown to be different approximations of the same BDMPS–Z path integral. In the opacity expansion, the hard scattering tail of the scattering potential of the medium is taken into account, but the interference between neighboring scattering centers is only taken into account order by order in the expansion. The most commonly used approximation is the single hard scattering ($N = 1$) approximation which assumes that there is only one dominant hard scattering. The multiple-soft scattering approximation resums all the interference terms, at the cost of neglecting hard scatterings with the medium. In general, the multiple-soft scattering approximation is expected to be valid for thick media, while the single-hard scattering approximation is more accurate for thin media.

2. *AMY vs multiple soft scattering approach*
   Parton energy loss within the AMY formalism can be formulated in terms of the same path integral entering the BDMPS–Z formalism [39]. The technical commonalities between both approaches are further elaborated in [45, 57]. The main conceptual difference between the AMY and the BDMPS-Z calculation is the formulation of the medium: an equilibrated high-temperature plasma in AMY versus static scattering centers in BDMPS-Z. There are also important technical differences, however. Most notably: in AMY an infinite-length medium is used, while BDMPS-Z includes finite-size effects in the emission rates. The effect of these differences is discussed in detail in [56]. In addition, the ASW calculation include the effect of large angle cut-off on the radiation. This effect is not taken into account in the standard AMY calculation, but is explored in detail in Section III C 3 below.

3. *Opacity expansions: DGLV vs ASW-SH*
   There are two implementations of the ($N = 1$) opacity expansion in the literature: DGLV [41, 46] and ASW–SH [38, 39]. Both groups calculate the same set of multiple scattering Feynman diagrams within the same high-energy and collinear approximation. However, in extending this result from the kinematic region in which these approximations are valid to the entire phase space open for gluon production, they take different approximations. The resulting numerical differences are discussed in detail in Section III B. In particular, large angle gluon

radiation is a source of significant theoretical uncertainty.

4. *Higher Twist vs Opacity Expansion*
   The Higher Twist formalisms and the ($N = 1$) Opacity expansion are related in the sense that they are formulated for media where the jet scatters a few times per emission. While both formalisms have extended the theoretical set-up to include multiple scatterings per emission, most comparisons to data still make use of the one scattering per emission approximation. This is referred to as leading order in opacity for GLV scheme and as next to leading twist in the higher twist scheme. The characterization of the medium is also somewhat different as the GLV scheme incorporates the full functional form for scattering off a heavy static scattering center and the HT scheme takes the leading transverse momentum moment of the exchanged transverse momentum distribution. The HT scheme thus assumes a Gaussian distribution for the exchanged transverse momentum.

   The formalisms differ significantly in the way multiple-gluon emission is treated. The Higher Twist calculation uses modified DGLAP virtuality evolution, while in the Opacity Expansion, multiple gluon emission is described using Poisson distributed independent emissions (see Section II B 4). The modified DGLAP evolution used in the HT scheme implies that subsequent radiated gluons are ordered in transverse momentum $k_\perp$ ($k_\perp$ of a given radiation is the upper bound for the subsequent radiation). There is no such restriction in the GLV scheme and each radiation may explore the limits set by the kinematic bounds.

D. Summary of the main findings

A detailed comparison of the different energy loss models touches on many aspects of the underlying phsyics assumptions, but also the technical implementation. Most of these aspects are mentioned in the preceding discussion and are treated in more detail in Section III. Here we list the four most important areas which are fundamental to the problem of radiative energy loss in a QCD medium.

1. *Effect of kinematic limits:*
   All formalisms make use of collinear approximation $\omega \gg k_T$. In addition, most of the calculations presented in Section III (ASW-SH, ASW-MS, GLV, and HT), except AMY, make use the soft radiation approximation $E \gg \omega$. In phenomenological calculations, we have to extend the calculations into the large-x, $\omega \to E$, and large-angle, $k_T \to \omega$, domain. For sufficiently large parton energies, the uncertainties associated with the large-x domain seem to be reasonably small (see Sections III B and III C). Large angle radiation, however, is expected to be problematic for all models. This is explored in detail in Section III B, for the opacity expansions, where the resulting uncertainty is found to be about a factor 2 in the gluon spectra. The resulting uncertainty in R_{AA} decreases with increasing p_T [54]. In Section III C it is shown that part of the difference between the AMY and ASW–MS formalism can be attributed to the absence of a large angle kinematic bound in the AMY calculation.

2. *Effect of treatment of multiple gluon emission:*
   In the existing formalisms, the calculation of the single-gluon emission kernel and the calculation of multiple gluon emission are separate steps. GLV, ASW-SH and ASW-MS use the Poisson ansatz; AMY uses rate equations; and HT uses DGLAP evolution. We find that differences between the energy loss formalisms originate at the single-gluon level. It is possible that the differences between the multiple-gluon emission treatment further affect the total energy loss, but we have not investigated this in detail. Semi-inclusive observables, like the fragmentation function or the jet shape, are expected to be more sensitive to the details of multiple gluon emission, such as whether the gluons are emitted independently (Poisson ansatz) or in a k_T ordered pattern (DGLAP evolution), than the leading particle energy loss or the single hadron suppression R_{AA}.

3. *Effect of medium model:*
   In most of the current energy loss formalisms, the picture of the medium is intrinsically tied to the approach used in the calculation. As a result, it is not possible to separate the effect of the medium model from assumptions made in the rest of the calculation. For example, the multiple-soft scattering calculation ASW-MS is only analytically feasible in the limit of gaussian broadening, which corresponds to scattering centers with a harmonic oscillator potential. On the other hand, the AMY approach uses a medium based on Hard Thermal Loop field theory with dynamical scattering centers. Futher work is required to systematically compare different medium models.

4. *Effect of including vacuum radiation:*
   All formalisms include vacuum radiation to some extent, except AMY. The fact that AMY shows the largest suppression in the final comparison (Section IV) is mostly due to lack of finite length effects. These effects lead to the L^2 dependence of energy loss during the early stage of the evolution. At later times, or larger L, this turns into a linear dependence on L. Because AMY implicitly assumes an infinite medium the L^2 dependence is lost. This behavior is studied in detail in [56] using the light cone path integral formalism including finite length

effects. The obtained rates show the expected L^2 dependence of the energy loss early in the evolution and approach the AMY result at late times.

Before we end this Section, we emphasize a common limitation of all formalisms of parton energy loss discussed here: They assume that the hadronization of the leading parton occurs in vacuum. The formalisms describe the interaction of the leading parton with the medium strictly at the partonic level, but do not consider any influence of the medium on the hadronization process or final-state interactions of the produced leading hadron with the medium. This appears to be justifiable for leading hadrons with momentum $p_h \gg m_h$, where m_h is the hadron mass, because the formation time for such a hadron is Lorentz dilated by a factor $p_h/m_h \gg 1$, and thus the formation of the hadron may be assumed to occur far outside the medium. Indeed, as discussed in the introduction, experimental evidence supports this assumption for light hadrons. We note however that this assumption is not generally satisfied under present conditions of heavy ion collisions at RHIC for baryons and mesons containing heavy quarks.

E. Directions for future work

It is clear from the preceding discussion that the current energy loss calculations have a number of specific weaknesses which may have large quantitative impact on the results. Based on our review of the existing models, we can formulate a number of questions for future work.

Firstly, we recommend to develop calculations with better control of the large angle and large energy radiation. In a realistic calculation, the radiation cross section should naturally go to zero at the kinematic limits $k_T = \omega$ and $\omega = E$. It is most important to control the large-angle behaviour; the large-energy regime can to some extent be avoided by concentrating on high-energy partons/jets. The most natural way to control the large-angle behaviour of the radiation would be to use the full Next-to-Leading Order (NLO) matrix elements for $2 \to 3$ scattering with radiation.

The treatments for multiple gluon radiation should also be further investigated. So far, the treatments are based on incoherent superposition and/or k_T-ordering of the shower. It is worthwhile to quantitatively investigate deviations from these assumptions. Semi-inclusive observables such as fragmentation functions and jet shapes may be more suitable to investigate specific multi-gluon emission scenarios than inclusive observables, such as the nuclear modification factor R_{AA}.

III. DETAILED COMPARISONS OF MODELS

In the following sections, we will present more detailed side-by-side comparisons of the existing energy loss formalisms. The discussion follows the structure layed out in Section II C.

A. The ASW formalism

As discussed in Section II B 2, the ASW formalism calculates parton energy loss based on a path-integral formalism [38–40] which can be evaluated either in the multiple soft scattering limit or through an opacity expansion. The GLV $N = 1$ opacity result reproduces the ASW expression [38] on the level of the Feynman diagrams and the analytic expression for the ω- and k_T-differential gluon energy distribution.

In this section, we concentrate on the multiple soft scattering approximation ASW–MS, which has been mostly used in comparisons to experimental data. A comparison of the single-hard scattering result ASW–SH to the DGLV opacity expansion [46] used by WHDG [47] is given in Section III B.

1. Gluon radiation spectrum

The result of the ASW–MS calculation is publicly available in terms of the 'quenching weights' which represent the energy loss probability distribution [58]. However, before discussing the probability distribution, we will present the single gluon radiation spectra. The multiple soft scattering limit suppresses the production of infrared gluons by a destructive interference effect. As a consequence, all spectra are peaked at finite gluon energies. In general, the radiated gluons become harder as one increases the average energy loss (i.e. as one increases $\hat{q}$). If the projectile energy is sufficiently large and the in-medium pathlength is sufficiently small, then the radiated gluons carry small fractions of the projectile energy. This is the case for a projectile quark energy $E = 100$ GeV shown in the upper panel of Fig. 3.

However, if the projectile energy is too small, see lower panel of Fig. 3, one faces a particular problem: One calculates the radiated gluon spectrum as if the parton would propagate through a medium of path-length L, although there is a finite probability that the parton does not have sufficient initial energy to make it through L, and gets stuck before. In the present calculational framework, finding yield in the spectrum beyond the kinematic boundary $x = 1$ ($\omega = E$), signals that one has assumed that the particle propagates through a length L for which the probability of 'death before arrival' is finite.

2. Multiple gluon emission

In the small x limit, the gluon emission probability is independent of the incident parton energy. In this case one may convolute with the Poisson distribution to

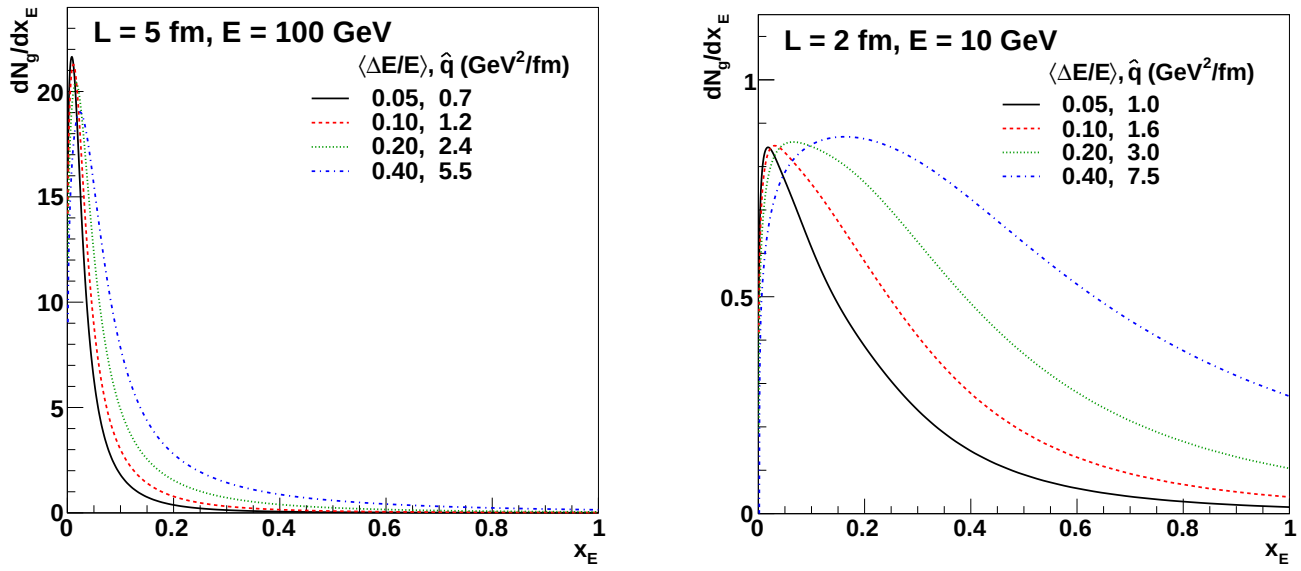


FIG. 3: Energy spectrum of radiated gluons, for a light quark with energy $E = 100$ GeV and path length $L = 5$ fm (top panel) and for a light quark with $E = 10$ GeV and $L = 2$ fm (lower panel). The legends on the plots indicate the average energy loss and the corresponding value of the transport coefficient $\hat{q}$.

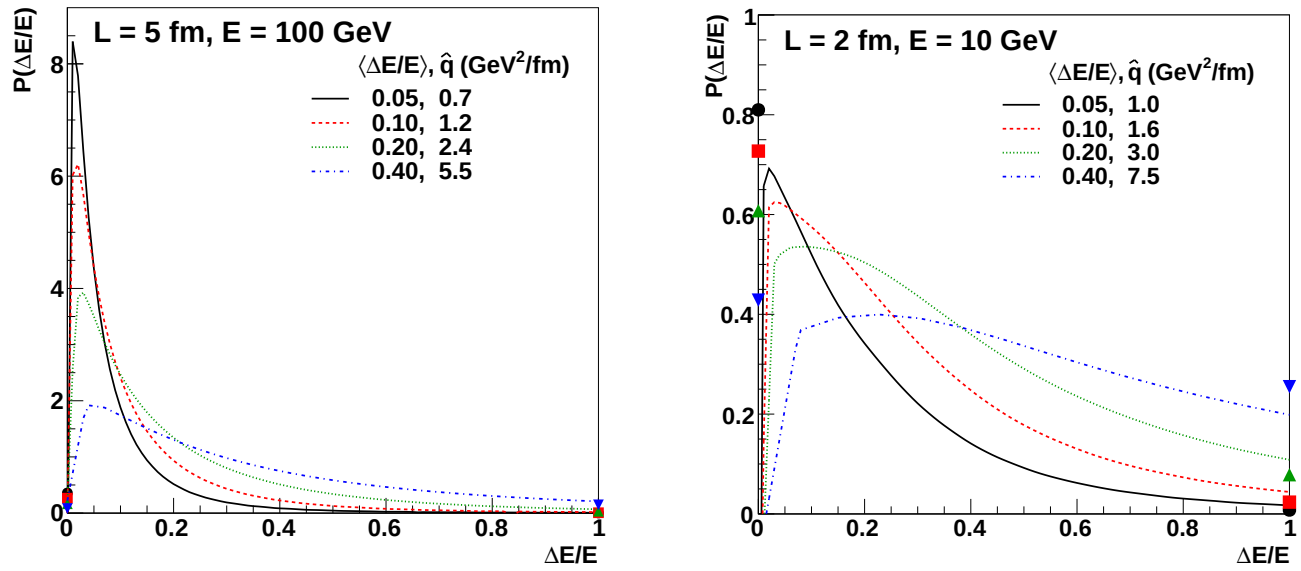


FIG. 4: Energy loss probability density $P(\Delta E)$ for a light quark of energy $E = 100$ GeV and path length $L = 5$ fm (top panel) and $E = 10$ GeV and $L = 2$ fm. The different lines are for different average energy loss, as indicated in the legend, together with the corresponding values of the transport coefficient $\hat{q}$.

compute the probability $P(\Delta E)$ for an incident parton to lose energy ΔE during its passage through the medium

$$P(\Delta E) = \sum_{n=0}^{\infty} \frac{e^{-\langle N_g \rangle}}{n!} \prod_{i=1}^{n} \left[\int d\omega \frac{dI}{d\omega} \right] \delta(\Delta E - \sum_{i=1}^{n} \omega_i) \,, \quad (1)$$

where $\langle N_g \rangle = \int_0^\infty d\omega (dI/d\omega)$ is the mean number of radiated gluons. This Poisson convolution is used in the ASW calculations for the multiple soft gluon approximation as well as the opacity expansion, and also in the GLV-based opacity expansions.

The resulting energy loss probability distribution

$P(\Delta E/E)$ are shown in Fig. 4 using the ASW multiple soft scattering limit for an incoming quark with energy E and in-medium path length L. All results have been computed with $\alpha_s = 0.3$. The probability distribution has three distinct pieces:

1. *Untouched survival*: There is finite probability that a parton does not interact with a medium of length L and that it loses no energy. This probability is $P(0) = \exp(-\langle N_g \rangle)$ and is represented by a color-coded dot at $\Delta E/E = -0.05$ in Fig. 4.

2. *Survival with finite energy loss*: This is the continuous probability that a parton makes it through a medium of length L but loses a finite fraction $\Delta E/E$ during its passage. This is denoted by the color-coded curve at finite $0 \leq \Delta E/E \leq 1$.

3. *Death before arrival*: In general, if one shoots a particle into a wall of thickness L, it can get stopped on its journey before reaching the length L. This probability is denoted by the color-coded dot at $\Delta E/E = 1.05$.

In general, as the average energy loss grows due to an increase in $\hat{q}$, one observes that:

(a) the probability of untouched survival decreases;

(b) the probability of survival with finite energy loss shifts to larger values of $\Delta E/E$;

(c) the probability of death before arrival increases.

This is seen clearly in Fig. 4, which shows the energy loss probability distribution $P(\Delta E/E)$ for two different choices of the parton energy E and path length L. The extreme case is $E = 10$ GeV and $L = 2$ fm (lower panel of Fig. 4), where requiring an energy loss of $\Delta E = 4$ GeV amounts to a greater than 40 percent probability of untouched survival and 30 percent probability of death before arrival. This comes close to an all-or-nothing scenario, where a particle either goes through without medium modification or gets stuck, but its probability of emergence as an object with reduced energy is relatively small.

3. *Uncertainties associated with kinematic limits*

The limitations of the high-energy eikonal approximations used in the derivation of the path-integral formalism from which both the multiple soft scattering limit and the opacity expansion stem, were discussed in the original papers [38–40]. More recently, ASW have used a number different approaches which are trying to address the shortcomings of the analytical calculations, such as using DGLAP evolution equations [59] and Monte Carlo algorithms for final state radiation [60–63].

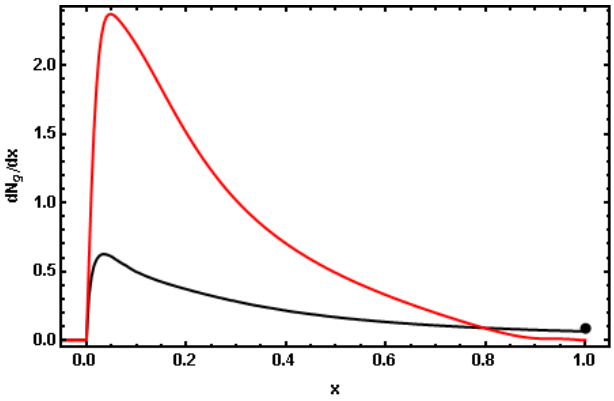


FIG. 5: Single inclusive gluon radiation distribution, dN_g/dx, from the WHDG implementation of the first order in opacity DGLV formula, Eq. (2), in red, and the ASW–SH implementation of Eq. (3), in black, for a 10 GeV up quark traversing a nominal, 2 fm long static brick of QGP held at a constant $T = 485$ MeV. The point at $x = 1$ indicates the integrated weight of dN_g/dx in the ASW–SH implementation for $x > 1$.

B. Opacity expansion: WHDG and ASW–SH

This subsection contains a detailed comparison of the radiative part of the WHDG calculation [47], equivalent to the first term in the DGLV opacity expansion [46], and the ASW opacity expansion formalism truncated to first order in opacity, here called ASW–SH [39, 40]. We discuss the importance of the definition of the splitting variable x and of the kinematic cut-offs made to enforce the assumptions used in deriving the energy loss formulae. Quantitative results comparing the radiative components of WHDG and ASW–SH will also be shown.

1. *Single emission kernel*

One of the major driving forces of the present investigation was the realization that some of the approximations made to arrive at analytical results for the medium-induced radiation have a larger impact on the final result than expected. An excellent case in point comes when one attempts a naive comparison between the single inclusive gluon distribution implemented in a massless quark and gluon version of the radiative piece of WHDG and the one found from the ASW–SH code [39, 58] for the opacity expansion. Both purport to compute the single inclusive distribution of gluon radiation, dN_g/dx, to first order in opacity [38, 41, 42] for a medium of Debeye-screened colored static scattering centers [11]. See Fig. 5, which shows $dN_g^{\rm DGLV}/dx$ and $dN_g^{\rm ASW-SH}/dx$ for a nominal 10 GeV quark jet in a static plasma of length 2 fm and temperature $T = 485$ MeV [84].

The DGLV formula for the first order in opacity energy loss is [46]:

$$x\frac{dN_g^{\rm DGLV}}{dx} = \frac{2C_R\alpha_s}{\pi^3}\frac{L}{\lambda}\int d^2\mathbf{q}d^2\mathbf{k}\frac{\mu^2}{\left(\mathbf{q}^2+\mu^2\right)^2}\frac{\mathbf{k}\cdot\mathbf{q}(\mathbf{k}-\mathbf{q})^2-\beta^2\mathbf{q}\cdot(\mathbf{k}-\mathbf{q})}{\left[(\mathbf{k}-\mathbf{q})^2+\beta^2\right]^2\left(\mathbf{k}^2+\beta^2\right)}\int dz\left[1-\cos\left(\frac{(\mathbf{k}-\mathbf{q})^2+\beta^2}{2xE}z\right)\right]\rho(z). \tag{2}$$

Here $\mathbf{q}$ is the transverse momentum exchanged with the medium and $\mathbf{k}$ the transverse momentum of the radiated gluon, μ is the Debeye screening mass, m_g and M_q are the effective thermal mass of the radiated gluon and the mass of the parent parton, respectively, $\beta^2 = m_g^2 + x^2M_q^2$; λ is the mean free path of the radiated gluon and $\rho(z)$ is the probability distribution for the distance to the first scattering center [85]. The equivalent expression for ASW–SH, which does not include the effect of a thermal gluon mass m_g, is [40]

$$\omega\frac{dI^{\rm ASW-SH}}{d\omega} = \frac{2C_R\alpha_s}{\pi^3}\frac{L}{\lambda}\int d^2\mathbf{q}d^2\mathbf{k}\frac{\mu^2}{(\mathbf{q}^2+\mu^2)^2}\frac{\mathbf{k}\cdot\mathbf{q}(\mathbf{k}-\mathbf{q})^2-x^2M_q^2\mathbf{q}\cdot(\mathbf{k}-\mathbf{q})}{\left[(\mathbf{k}-\mathbf{q})^2+x^2M_q^2\right]^2\left(\mathbf{k}^2+x^2M_q^2\right)}$$
$$\times\int dz\left[1-\cos\left(\frac{(\mathbf{k}-\mathbf{q})^2+x^2M_q^2}{2\omega}\right)\right]\rho(z). \tag{3}$$

If we set $\omega = xE$ in (3) and $m_g = 0$ in β in (2), then we see that Eqs. (2) and (3) are, in fact, identical. Why, then, do the curves obtained by evaluating these expressions, shown in Fig. 5, differ so drastically? The answer lies in the details of the implementation of these two expressions. It turns out that there are a number of choices that must be made in going from the differential expressions for the radiation spectrum to the integrated gluon distribution, dN_g/dx. These are summarized in Table I.

	WHDG	ASW–SH
$k_{\rm max}$	$2x(1-x)E$	xE
x	x_+	$x_{\rm E}$
$q_{\rm max}$	$\sqrt{3\mu E}$	∞
$\rho(z)$	$2e^{-2z/L}\theta(z)/L$	$\theta(L-z)\theta(z)/L$
L/λ	$L\rho\sigma = L\rho\times 9\pi\alpha_s^2/(2\mu^2)$	1
α_s	0.3	1/3
m_g; M_q	$\mu/\sqrt{2}$; $\mu/2$	0; 0

TABLE I: Table of differences between the implementations of Eqs. (2) and (3) in WHDG and in ASW–SH.

The differences outlined in Table I have been individually explored to see which choices have a large effect on the calculated gluon spectra. The effect of non-zero quark mass M_q is small, because the mass is small compared to the total energy. The choices for α_S differ by 10% which directly translates into a change in the single gluon spectra by the same amount. The shape of the distribution also depends on α_S through the value of μ, but this is a small effect. It also turns out that the choice of $q_{\rm max}$ has only a small effect, because of the small radiation probability for $q > \sqrt{3\mu T}$. Another small effect is the choice of $\rho(z)$; the difference between the exponential profile and a uniform density only leads to characteristic shapes in the spectrum for small $L \lesssim 2$ fm, but does not effect the total radiation probability much. The effect of

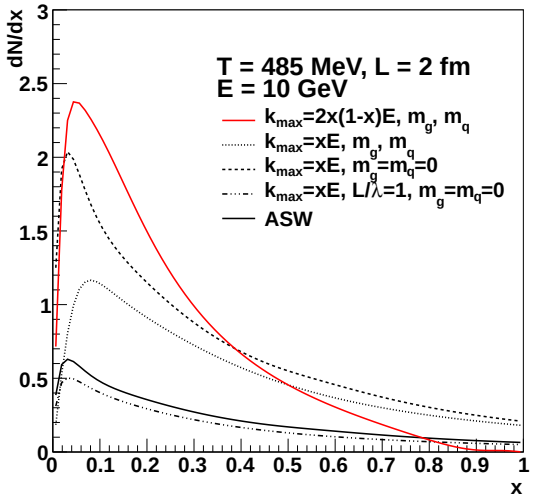


FIG. 6: Comparison of the single gluon emission spectrum for several variants of the $N = 1$ opacity expansion, using a uniform medium with $T = 485$ MeV and $L = 2$ fm. All curves use $\alpha_S = 0.3$ and $q_{\rm max} = 10$ GeV $\gg \sqrt{3\mu E}$. The solid curve labeled ASW corresponds to what is used in [39, 40], while the grey (red) curve corresponds to the radiative WHDG formalism used in [46, 47], except for the difference in $q_{\rm max}$. See text for details.

the density profile $\rho(z)$ on the gluon spectrum can be seen in Fig. 6, comparing the lower solid line, labeled ASW, which uses $\rho(z) = \Theta(L-z)/L$ and the dot-dot-dashed line using $\rho(z) = 2\exp(-2z/L)/L$.

The remaining three items in Table I have significant effects on the gluon radiation spectrum. The effect of each of these on the gluon spectrum is show in Fig. 6. L/λ enters as a multiplication factor in the single gluon spectrum (compare dot-dot-dashed and dashed line). This is a significant factor at $T = 485$ MeV,

$\lambda = 0.62$ fm. The choice of $L/\lambda = 1$ in the ASW papers [40] was made for convenience in tabulating the quenching weights $P(\Delta E)$, but this calculation has never been used to determine the medium density. In the rest of this paper, we will therefore include L/λ different from unity in the calculation. Introduction of a finite gluon mass m_g leads to a sizable reduction of the radiation at small x where $\omega \approx m_g$ (compare dashed and dotted lines in Fig. 6). On the other hand, due to nontrivial interference effects, its effect on observables such as R_{AA} is actually not very large [54].

Finally, the choice of the cut-off k_{max} on the perpendicular component of the gluon momentum has a large effect, mostly at small x, where the difference between the cut-offs is a factor 2 and the probability of radiation at finite $k_\perp$ is large (compare dotted line and solid grey (red) line in Fig. 6). Because this cut-off is also related to large angle radiation, it has a fundamental impact on our ability to calculate the radiation spectrum, which we will discuss in more detail in the following section.

2. Definition of the variable x

The upper bound of the transverse gluon momentum $k_\perp$ is different in the WHDG calculation than in the ASW–SH calculation. At small x, both formalisms implement a cut to ensure forward emission of the gluon. The difference in the values of the cut-off arises because in the derivations descending from the work by GLV[41, 42, 46, 64], x is taken to be the positive light-cone momentum fraction $x = x_+ = k^+/P^+$, while the ASW–SH derivation [38, 40] uses $x = x_{\rm E} = k^0/P^0$, the fraction of energy carried away by the radiated gluon.

If we denote the usual four-momenta with parentheses and light-cone momenta with brackets then the radiated gluon four-momentum is

$$\begin{aligned} k &= \left(x_{\rm E}E, \mathbf{k}, \sqrt{(x_{\rm E}E)^2 - \mathbf{k}^2}\right) \\ &= \left[x_+E^+, \frac{\mathbf{k}^2}{x_+E^+}, \mathbf{k}\right], \end{aligned} \tag{4}$$

where $\mathbf{k}$ is the momentum of the gluon transverse to the direction of the parent parton and the gluon is assumed to be on mass shell.

In light-cone coordinates forward emission implies that $k^+ > k^-$. This condition implies

$$k_T < k_{\rm max} = x_+P^+ = x_+E^+. \tag{5}$$

For a massless parent parton, $E^+ = 2E$, so that $k_{\rm max} = 2x_+E$. In Minkowski coordinates forward emission implies that $k_z > 0$. This condition implies

$$k_T < k_{\rm max} = \omega = x_{\rm E}E. \tag{6}$$

Both values of $k_{\rm max}$ restrict emission to angles be less than 90°, which is still a rather wide angle. In general, a cut-off angle $\theta_{\rm max}$ can be defined, leading to

$$k_{\rm max} = \begin{cases} x_+E^+\tan(\theta_{\rm max}/2), & x = x_+, \\ x_{\rm E}E\sin(\theta_{\rm max}), & x = x_{\rm E}. \end{cases} \tag{7}$$

Note that the same physical cut-off at an angle $\theta_{\rm max}$ gives different expression for $k_{\rm max}$ as a function of x_E and x_+. The exact relations between x_+ and $x_{\rm E}$ are

$$x_+ = \frac{1}{2}x_{\rm E}\left(1 + \sqrt{1 - \left(\frac{k_T}{x_{\rm E}E}\right)^2}\right), \tag{8}$$

$$x_{\rm E} = x_+\left(1 + \left(\frac{k_T}{x_+E^+}\right)^2\right). \tag{9}$$

Note that to lowest order in the expansion parameter is k_T/xE, which controls the extent of collinearity, the two definitions of x are identical. The difference between using x_E and x_+ in the calculations is only significant at larger angles.

3. Transverse momentum cut-off at large momentum fraction

Eqs. (2) and (3) also have support for all values of x. Nonzero weight in dN_g/dx for $x > 1$ of course violates energy-momentum conservation. Requiring the continued forward propagation of the parent parton leads to an additional k_T cut-off that enforces energy-momentum conservation and also restricts large-angle radiation at large x.

The momentum of a massless parent parton after energy loss is

$$\begin{aligned} p &= \left((1-x_{\rm E})E, \mathbf{q}-\mathbf{k}, \sqrt{\left((1-x_{\rm E})E\right)^2 - \left(\mathbf{q}-\mathbf{k}\right)^2}\right) \\ &= \left[(1-x_+)E^+, \frac{(\mathbf{q}-\mathbf{k})^2}{(1-x_+)E^+}, \mathbf{q}-\mathbf{k}\right], \end{aligned} \tag{10}$$

where $\mathbf{q}$ is the transverse momentum transfer to the parent parton from the scattering center. For completeness the original parent parton momentum is $P = (E, \mathbf{0}, E) = [E^+, 0, \mathbf{0}]$.

In light-cone coordinates, forward propagation of the final state parton implies $p^+ > p^-$; in Minkowski coordinates it implies $k_z > 0$. For the light-cone coordinate case forward propagation leads to

$$(1-x_+)E^+ > |\mathbf{q}-\mathbf{k}| \approx k_T, \tag{11}$$

where $|\mathbf{q}| \sim 3T < q_{\rm max} = \sqrt{6ET}$ is small compared to most values of $|\mathbf{k}|$; for the Minkowski coordinate case forward emission leads to

$$(1-x_{\rm E})E > |\mathbf{q}-\mathbf{k}| \approx k_T. \tag{12}$$

For each definition of x there are two cut-offs (e. g. Eqs. (5) and (11) for $x \equiv x_+$ or Eqs. (6) and (12) for

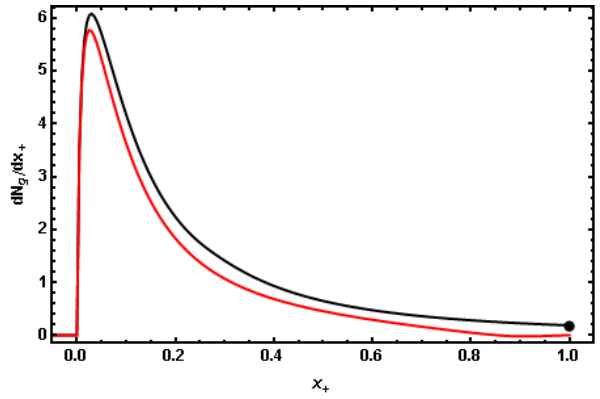


FIG. 7: Single gluon spectra using Eq. (2) with $k_{\max} = x_+E^+$ (black) and $k_{\max} = x_+(1-x_+)E^+$ (red) cut-offs for a 10 GeV up quark traversing a 2 fm static QGP of $T = 485$ MeV and $m_q = m_g = 0$. The black dot at $x_+ = 1$ represents the integrated weight of dN_g/dx_+ for $x_+ > 1$ when $k_{\max} = x_+E^+$.

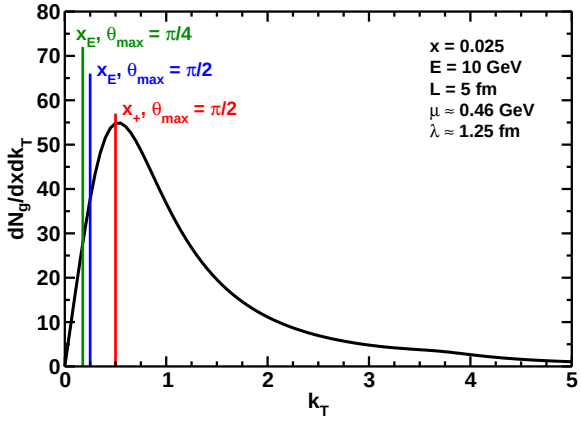


FIG. 8: Transverse momentum spectrum $dN_g/dxdk_T$ of emitted gluons with $x = 0.025$, calculated using Eq. (2) for a light quark with all masses set to 0, $E = 10$ GeV, $L = 5$ fm, and representative values of $\mu \approx 0.46$ GeV and $\lambda \simeq 1.25$ fm for a medium density of $dN_g/dy = 1000$ similar to RHIC conditions [47]. Vertical lines depict the three values of k_T discussed in the text as possible cut-offs to enforce collinearity in Eq. (2).

$x \equiv x_{\rm E}$); this needs to be taken into account when evaluating the k_T integral over $dN_g/dxdk_T$. One possibility would be to take the minimum of the two definitions; for instance, using light-cone coordinates and taking $\theta_{\max} = \pi/2$; this would mean $k_{\max} = \min(x_+, 1-x_+)E^+$. The present implementations of DGLV and WHDG use a smoother function, $k_{\max} = x_+(1-x_+)E^+$. Note that the existing ASW–SH implementation [39, 58] does not include a large-x cut-off.

Figure 7 shows the single gluon spectra dN/dx_g with the two different cut-offs Eq. 5 and Eq. 11. It can be seen in the Figure that the effect of introducing the kinematic cut-off $x \leq 1$ is small in regimes where the dN_g/dx peak is large and at small x, for instance for $L = 2$ fm, with the effective gluon mass set to zero, $m_g = 0$. In this sense the $dN_g/dxdk_Tdq_T$ integrand respects the small-x approximation rather well. In Fig. 6 the effect of lifting the $x \leq 1$ kinematic cut-off is more important because the number of radiated gluons $\langle N_g \rangle$ is smaller when $m_g \neq 0$; in this case the large-x cut-off causes a 10-20% change in $\langle N_g \rangle$. In general, the effect of the large-x cut-off is expected to increase with increasing path length and to decrease with increasing parton energy.

4. *Effect of large angle radiation*

In order to illustrate the sensitivity of the single gluon emission probability to $k_{\max}$, Fig. 8 plots $dN_g/dxdk_T$ for $x = 0.025$, along with an illustration of three possible cut-offs for k_T:

(a) $x = x_+$ with $\theta_{\max} = \pi/2$;
(b) $x = x_{\rm E}$ with $\theta_{\max} = \pi/2$;
(c) $x = x_{\rm E}$ with $\theta_{\max} = \pi/4$.

Recall that to lowest order in collinearity, the first two cut-offs are identical; the third is a natural $\mathcal{O}(1)$ variation in the cut-off that one can use to estimate the systematic uncertainties deriving from the collinear approximation. Clearly the assumption of collinearity is badly violated: for values of $x \sim \mu/E$, $dN_g/dxdk_T$ reaches its maximum value at $k_T \sim xE$. For these values of x the emission spectrum is highly sensitive to the choice of $k_{\max}$: $dN_g/dx \sim k^2_{\max}$.

Since the collinear approximation is so badly broken, it is not a good approximation to take $x_+ \approx x_{\rm E}$. A meaningful comparison of results, then, can come only when the emission spectra of Eqs. (2) and (3) are plotted with respect to the same variables. Since one is interested in a differential quantity, a Jacobian is required. We choose to transform x_+ to $x_{\rm E}$ because, ultimately, one is interested in energy loss, as opposed to the loss of positive light-cone momentum. The transformed spectrum is then given by

$$\frac{dN_g^{\rm J}}{dx_{\rm E}}(x_{\rm E}) = \int^{k_{\max}} dk_T \frac{dx_+}{dx_{\rm E}} \frac{dN_g}{dx_+ dk_T}\big(x_+(x_{\rm E})\big), \qquad (13)$$

with

$$\frac{dx_+}{dx_{\rm E}} = \frac{1}{2}\left[1 + \left(1 - \left(\frac{k_T}{x_{\rm E}E}\right)^2\right)^{-1}\right], \qquad (14)$$

$$k_{\max} = x_{\rm E}E\sin(\theta_{\max}). \qquad (15)$$

Note the change in the upper limit (15) of integration in Eq. (13). The resulting comparison of $dN_g/dx_{\rm E}$ is shown in Fig. 9. Note the very large difference in the results for the two collinearly equivalent definitions of x and that for the result with a reduced $\theta_{\max}$. Of course this enormous difference implies a large (factor $2-3$) uncertainty in the extraction of the medium parameters from leading hadron suppression data [54].

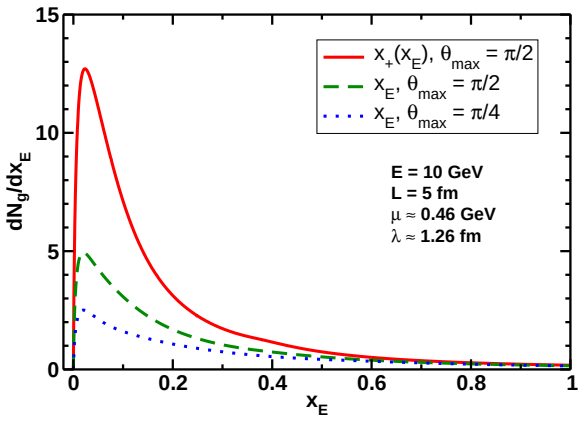


FIG. 9: Comparison of Eqs. (2) and (3) in the massless limit and for which the x_+ dependence of Eq. (2) has been transformed into $x_{\rm E}$; see Eq. (13). Also shown is the result when using the $x_{\rm E}$ interpretation and reducing $\theta_{\rm max}$ to $\pi/4$, a reasonable $\mathcal{O}(1)$ variation in the k_T cut-off.

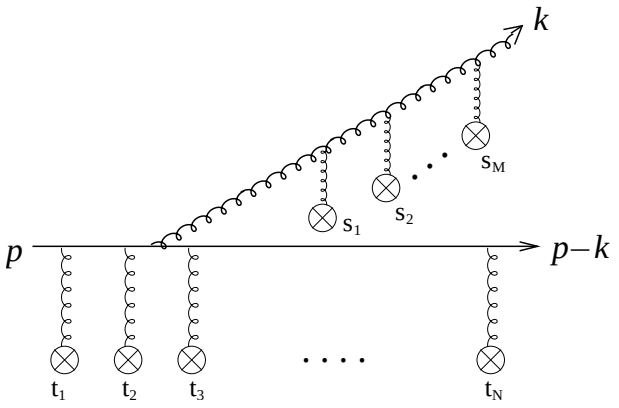


FIG. 10: A typical diagram calculated in the AMY and BDMPS–Z approaches.

C. AMY, BDMPS–Z and ASW–MS

1. *AMY transport equations*

The medium-induced radiative energy loss suffered by high energy partons passing through nuclear matter was first computed in the BDMPS–Z approach [12, 34–37], in which the gluon emission probability is expressed in terms of the Green's function of a 2-D Schrödinger equation with an imaginary potential proportional to the interaction cross section with color centers of a quark-antiquark-gluon system.

In the AMY approach [51, 52, 65, 66], the gluon emission rates are calculated fully at leading order in α_s by resumming an infinite number of ladder diagrams in the context of hard thermal loop resummed QCD. Both approaches are valid in the multiple soft scattering limit, but differ in several essential ways: in AMY the medium consists of fully dynamic thermal quarks and gluons, while in BDMPS–Z the medium is treated as a collection of static scattering centers. In BDMPS–Z the gluon emission probability is calculated in configuration space while in AMY the radiation rate is calculated in momentum space. Salgado and Wiedemann [39] further extended the BDMPS–Z formalism to include the correct thin plasma limit, which has important quantitative effects. In addition, different evolution schemes are used for multiple-gluon emission: the AMY formalism uses rate equations to obtain the final parton distributions while applications of the BDMPS–Z calculation convolute the radiation rate with a Poisson distribution to obtain the quenching weights.

The main assumption in these two formalisms is that the temperature of the medium is high enough such that the asymptotic freedom of QCD makes it possible to treat the interactions between a fast parton and the medium using perturbation theory. In this case, soft exchanges between the medium and the propagating parton dominate the stimulated radiation of a hard collinear gluon. At the same time, the effect of multiple collisions is reduced due to the coherence between multiple soft scatterings within the formation time of the emitted gluon (LPM effect). This effect makes it necessary to resum all diagrams as depicted in Fig. 10 to calculate the leading order gluon emission probability/rate.

In the AMY approach, one considers a hard parton traversing an extended medium in thermal equilibrium with asymptotically high temperature $T \to \infty$. Due to the small coupling $g \to 0$, a hierarchy of parametrically separated scales $T > gT > g^2T$ makes it possible to construct an effective field theory of soft modes (modes with momentum $|\mathbf{k}| \sim gT$) by summing contributions from hard thermal loops into effective propagators and vertices [67, 68]. The hard parton traversing a thermal QGP undergoes a series of soft elastic scatterings with transverse momentum of order $\sim gT$ off the thermal particles of the medium. The differential cross section (interaction rate) at leading order in α_s is

$$\frac{d\bar{\Gamma}_{\rm el}}{d^2q_\perp} = \frac{1}{(2\pi)^2}\frac{g^2Tm_{\rm D}^2}{\mathbf{q}_\perp^2(\mathbf{q}_\perp^2+m_{\rm D}^2)}\,. \tag{16}$$

Note that the rate has been divided by the quadratic color Casimir C_R of the parent parton, indicated by placing a bar over the rate $\Gamma_{\rm el}$ (similarly for other quantities).

These soft multiple scatterings induce collinear splitting of partons. The time scale over which the parton and emitted gluon overlap is of order $\sqrt{\omega/\hat{q}}$, which is of greater or equal order of magnitude than the mean free time of soft scatterings for $\omega \geq T$, with ω the energy of the radiated gluon. To obtain the leading-order gluon emission rates, one must consistently take into account the multiple scattering processes. Within the thermal field theory, one essentially calculates the imaginary parts of an infinite number of gluon self-energy ladder diagrams. The resummation of these ladder diagrams can be organized into a Schwinger-Dyson type equation for

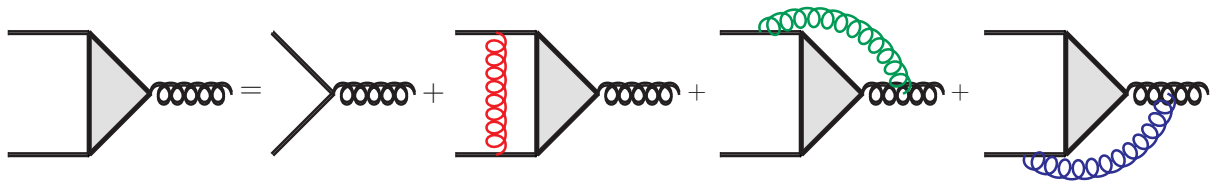


FIG. 11: Diagrammatic representation of the Schwinger-Dyson equation for the emission vertices.

the dressed radiation vertex, as depicted in Fig. 11. The corresponding integral equation is

$$\begin{aligned} 2\mathbf{h} &= i\,\delta E(\mathbf{h},p,k)\mathbf{F}(\mathbf{h}) + \int d^2q_\perp \frac{d\bar{\Gamma}_{\rm el}}{d^2q_\perp} \\ &\times \Big[(C_s - C_{\rm A}/2)[\mathbf{F}(\mathbf{h}) - \mathbf{F}(\mathbf{h}-k\,\mathbf{q}_\perp)] \\ &+(C_{\rm A}/2)[\mathbf{F}(\mathbf{h}) - \mathbf{F}(\mathbf{h}+p\,\mathbf{q}_\perp)] \\ &+(C_{\rm A}/2)[\mathbf{F}(\mathbf{h}) - \mathbf{F}(\mathbf{h}-(p-k)\,\mathbf{q}_\perp)]\Big]\,. \end{aligned} \tag{17}$$

In the above equation, δE is the energy difference between the initial and final states,

$$\begin{aligned} \delta E(\mathbf{h},p,k) &= E_{p-k} + E_k - E_p \\ &= \frac{\mathbf{h}^2}{2pk(p-k)} + \frac{m_k^2}{2k} + \frac{m_{p-k}^2}{2(p-k)} - \frac{m_p^2}{2p}, \end{aligned} \tag{18}$$

with p the incoming parton momentum and k the momentum of the radiated hard gluon. $1/\delta E$ is of order of the formation time for the bremsstrahlung process in the medium. The masses appearing in the above equations are the medium induced thermal masses. The 2-D vector $\mathbf{h}$ is a measure of non-collinearity of the final states, defined to be $\mathbf{h} \equiv (\mathbf{p}\times\mathbf{k})\times\mathbf{e}_{||}$, with $\mathbf{e}_{||}$ the unit vector along the chosen longitudinal direction; here $\mathbf{h}$ is parametrically of order $gTE(\omega/T)^{1/4}$ and therefore small compared to $\mathbf{p}\cdot\mathbf{k}$, with $\omega\sim k$. For the case of $g\to q\bar{q}$, the $(C_s - C_A/2)$ term is the one with $\mathbf{F}(\mathbf{h}-p\,\mathbf{q}_\perp)$ rather than $\mathbf{F}(\mathbf{h}-k\,\mathbf{q}_\perp)$ in the above equation.

The gluon emission rate $d\Gamma(p,k)/dk$ is obtained by closing off the dressed vertex with the bare vertex including the appropriate statistical factors,

$$\frac{d\Gamma(p,k)}{dk} = \frac{C_s g^2}{16\pi p^7}\frac{1}{1\pm e^{-k/T}}\frac{1}{1\pm e^{-(p-k)/T}} \times \left\{ \begin{array}{ll} \frac{1+(1-x)^2}{x^3(1-x)^2} & q\to qg \\ N_{\rm f}\frac{x^2+(1-x)^2}{x^2(1-x)^2} & g\to q\bar{q} \\ \frac{1+x^4+(1-x)^4}{x^3(1-x)^3} & g\to gg \end{array} \right\} \times \int \frac{d^2h}{(2\pi)^2} 2\mathbf{h}\cdot{\rm Re}\,\mathbf{F}(\mathbf{h},p,k)\,. \tag{19}$$

Here C_s is the quadratic Casimir relevant for the process ($C_F = 4/3$ for quarks or $C_A = 3$ for gluons), and $x\equiv k/p$ is the momentum fraction of the gluon (or the quark, for the case $g\to q\bar{q}$). The subsequent multiple emissions are treated by evolving the momentum distribution $P(p) = dN/dp$ of the traversing hard partons in a set of rate equations,

$$\frac{dP_{q\bar{q}}(p)}{dt} = \int_k P_{q\bar{q}}(p+k)\frac{d\Gamma^q_{qg}(p+k,k)}{dk} - P_{q\bar{q}}(p)\frac{d\Gamma^q_{qg}(p,k)}{dk} + 2P_g(p+k)\frac{d\Gamma^g_{q\bar{q}}(p+k,k)}{dk}\,, \tag{20}$$

$$\frac{dP_g(p)}{dt} = \int_k P_{q\bar{q}}(p+k)\frac{d\Gamma^q_{qg}(p+k,p)}{dk} + P_g(p+k)\frac{d\Gamma^g_{gg}(p+k,k)}{dk} - P_g(p)\left(\frac{d\Gamma^g_{q\bar{q}}(p,k)}{dk} + \frac{d\Gamma^g_{gg}(p,k)}{dk}\Theta(k-p/2)\right). \tag{21}$$

In the AMY approach, the medium consists of fully dynamic thermal quarks and gluons; the effect of emitting and absorbing thermal energy are fully included in the evolution equations. In addition, the elastic energy loss due to the recoil of the dynamical scattering centers can also be consistently included in the formalism [69, 70]. However, the transition rates are calculated in momentum space assuming the thermodynamic limit, i.e., the high energy parton experiences a uniform medium on the time scale of the formation time of the emitted radiation.

2. *Comparison of BDMPS–Z and AMY*

In the BDMPS–Z formalism, one calculates the amplitude for a quark-antiquark-gluon system evolving in the medium without inducing inelastic reactions (following Zakharov). The general formula for the probability of the gluon emission by a hard parton traversing the medium may be expressed as,

$$k\frac{dI}{dk} = \frac{\alpha x P_{s\to g}(x)}{[x(1-x)p]^2}{\rm Re}\int_0^\infty dt_1\int_{t_1}^\infty dt_2 \Big(\nabla_{\mathbf{b}_1}\cdot\nabla_{\mathbf{b}_2}[G(\mathbf{b}_2,t_2|\mathbf{b}_1,t_1) - G_{\rm vac}(\mathbf{b}_2,t_2|\mathbf{b}_1,t_1)]\Big)_{\mathbf{b}_1=\mathbf{b}_2=0}\,. \tag{22}$$

Here I is the probability of gluon bremsstrahlung from the high energy particle, $P_{s\to g}(x)$ is the vacuum splitting function for relevant process and $G(\mathbf{b}_2, t_2|\mathbf{b}_1, t_1)$ is the Green's function of a 2-D Schrödinger equation with Hamiltonian

$$H(\mathbf{p_b}, \mathbf{b}, t) = \delta E(\mathbf{p_b}) - i\Gamma_3(\mathbf{b}, t)\,. \tag{23}$$

The initial condition for the Green's function is

$$G(\mathbf{b}_2, t|\mathbf{b}_1, t) = \delta^2(\mathbf{b}_2 - \mathbf{b}_1). \tag{24}$$

The kinetic term in the Hamiltonian describes the energy difference between initial and final states, as given by Eq.(18), with $\mathbf{p_b} = \mathbf{h}/p$, and Γ_3 in the potential term is the 3-body interaction rate,

$$\begin{aligned}\Gamma_3(\mathbf{b}, t) \;=\; & \frac{1}{2}C_A\bar{\Gamma}_2(\mathbf{b}, t) + (C_s - \frac{1}{2}C_A)\bar{\Gamma}_2(x\mathbf{b}, t) \\ & + \frac{1}{2}C_A\bar{\Gamma}_2((1-x)\mathbf{b}, t)\,,\end{aligned} \tag{25}$$

where Γ_2 is related to the Fourier transform of the elastic collision rate $d\bar{\Gamma}_{\rm el}/d^2q_\perp$ by

$$\bar{\Gamma}_2(\mathbf{b}, t) = \int d^2q_\perp \frac{d\bar{\Gamma}_{\rm el}}{d^2q_\perp}\left(1 - e^{i\mathbf{b}\cdot\mathbf{q}_\perp}\right)\,. \tag{26}$$

Note that in the original BDMPS–Z formula, the rate $\bar{\Gamma}_{\rm el}$ for soft scatterings was written as the number density ρ of the static scattering centers in the medium times elastic cross section $\sigma_{\rm el}$ for such scatterings. Here we follow the notation of Arnold [57] and write BDMPS–Z formulas more generally in terms of the rate $\bar{\Gamma}_{\rm el}$ for elastic scatterings off the medium constituents. Since the medium is treated as a collection of static scattering centers, one replaces the denominator of Eq. (16) with $(\mathbf{q}_\perp^2 + m_D^2)^2$ for the elastic scattering rate. Further assuming that the gluon emission rate is dominated by the region $b \lesssim 1/m_D$, one may approximate the elastic rate by

$$\bar{\Gamma}_2(\mathbf{b}, t) = \frac{1}{4}\hat{\bar{q}}b^2\,, \tag{27}$$

where $C_R\hat{\bar{q}}$ is transverse momentum squared transferred to incident parton per unit time (C_R is the appropriate color factor for the parton). Neglecting the effective masses of the particles, the Hamiltonian takes the Harmonic oscillator form,

$$H(\mathbf{p_b}, \mathbf{b}, t) = \frac{p_b^2}{2M} + \frac{1}{2}M\omega_0^2 b^2\,, \tag{28}$$

where

$$\omega_0^2 = -i\frac{(1-x)C_A + x^2C_s}{2M}\hat{\bar{q}}\,, \tag{29}$$

and $M = x(1-x)p$. Making use of the oscillator Green's function and performing the integration over time t_1 and t_2 for a brick of medium with length L, one may obtain the BDMPS–Z formula for multiple-soft scattering,

$$k\frac{dI}{dk} = \frac{\alpha x P_{s\to g}(x)}{\pi}\ln|\cos(\omega_0 L)|\,. \tag{30}$$

The correspondence between Eq. 22, which is the starting point to derive the BDMPS–Z formula above, and Eq. 19, the rates calculated by AMY, has been explored by Aurenche and Zakharov for photon radiation [71] and by Arnold for gluon radiation [57]. Here we reproduce the main steps. First, note that the Green's function only depends on the time difference $\Delta t = t_2 - t_1$ due to time invariance. Performing the integral over t_1 which gives a factor of total time, the resulting non-vacuum part of Eq.(22) becomes

$$\begin{aligned}\frac{d\Gamma}{dk} \;=\; & \frac{\alpha P_{s\to g}(x)}{x^2(1-x)^2p^3} \\ & \times\; {\rm Re}\int_0^\infty d\Delta t\,\left[\nabla_{\mathbf{b}_1}\cdot\nabla_{\mathbf{b}_2}G(\mathbf{b}_2, \Delta t|\mathbf{b}_1, 0)\right]_{\mathbf{b}_1=\mathbf{b}_2=0}\,.\end{aligned} \tag{31}$$

One may define the time-integrated amplitude

$$\mathbf{f}(\mathbf{b}) = 2i\int_0^\infty dt[\nabla_{\mathbf{b}_1}G(\mathbf{b}, t|\mathbf{b}_1, 0)]_{\mathbf{b}_1=0}\,, \tag{32}$$

which satisfies the following equation,

$$-2\nabla_{\mathbf{b}}\delta^2(\mathbf{b}) = H\mathbf{f}(\mathbf{b})\,. \tag{33}$$

In terms of the amplitude $\mathbf{f}(\mathbf{b})$, the gluon emission rate becomes

$$\frac{d\Gamma}{dk} = \frac{\alpha P_{s\to g}(x)}{x^2(1-x)^2p^3}{\rm Re}[(2i)^{-1}\nabla_{\mathbf{b}}\cdot\mathbf{f}(\mathbf{b})]_{\mathbf{b}=0}\,. \tag{34}$$

Fourier transforming Eq. (33) from impact parameter space to momentum space with the use of Eq.(28), one obtains the linear integral equation [Eq.17], with $\mathbf{F}(\mathbf{h}) = p\mathbf{f}(\mathbf{p_b})$. The gluon emission rate becomes

$$\frac{d\Gamma}{dk} = \frac{\alpha P_{s\to g}(x)}{4x^2(1-x)^2p^7}\int\frac{d^2h}{(2\pi)^2}{\rm Re}[2\mathbf{h}\cdot\mathbf{F}(\mathbf{h})]\,. \tag{35}$$

Including the appropriate final state statistical factors, one reproduces the AMY formula (19) for the gluon emission rate.

3. Large angle radiation in AMY

In order to explicitly exclude large angle radiation, which is automatically suppressed for $g \ll 1$ but can contribute for larger g, we suppress the large angle contributions in the integral over $\mathbf{h}$ in Eq. 19 by introducing an envelope function $W(k_\perp, k_{\perp\max})$, where $k_\perp = h/p$.

A reasonable choice for W is a Gaussian that cuts off k_T above a value $k_{\perp\max}$. We choose a Gaussian because the integral equation Eq. 17 is solved by Fourier transforming into the so called impact parameter space (see

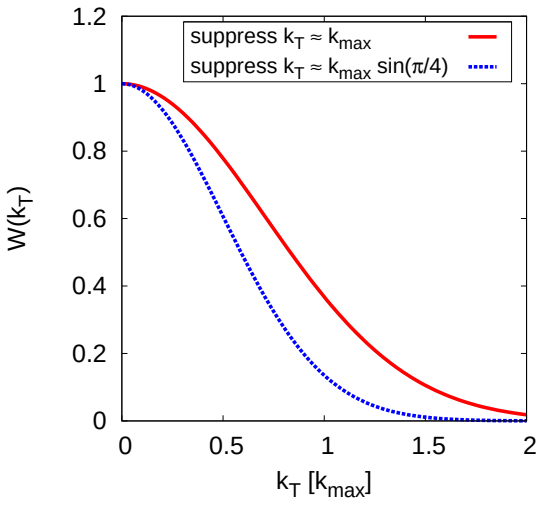


FIG. 12: (Color online) Envelope function W for different maximal transverse momenta.

[72]), where it becomes a differential equation. Hence, we want an envelope function whose Fourier transform is analytic and well behaved. Explicitly we define

$$W(k_\perp, k_{\perp\max}) = \exp(-k_\perp^2/k_{\perp\max}^2)\,, \tag{36}$$

where we can vary $k_{\perp\max}$, depending on how much we want to restrict the emission angle. First, we would like to exclude the $k_\perp$ that are kinematically disallowed, so we choose the following $k_{\perp\max}$:

$$k_{\perp\max}^2 = \begin{cases} k^2 & \text{for } |p| > |k| \text{ and } |p-k| > k \\ (p-k)^2 & \text{for } |p| > |k| \text{ and } |p-k| < k \\ (p-k)^2 & \text{for } |p| < |k| \text{ and } |p| > |p-k| \\ p^2 & \text{for } |p| < |k| \text{ and } |p| < |p-k| \end{cases} \tag{37}$$

This suppresses most of the kinematically disallowed $k_\perp$ and makes sure that $k_\perp$ is always smaller than the smallest momentum. Note again, that in the limit of $g \ll 1$ those kinematically disallowed transverse momenta are already suppressed, so that the formalism is perfectly consistent with kinematics in the limit where it is derived.

To also suppress $k_\perp$ which correspond to emission angles larger than a certain $\theta_{\max}$, we can replace $k_{\perp\max}$ by $k_{\perp\max}\sin(\theta_{\max})$. Fig. 12 shows the envelope function W for the original $k_{\perp\max}$ and for a maximal emission angle of $\theta_{\max} = \pi/4$. Using a Gaussian, not all contributions from $k_\perp > k_{\perp\max}$ are removed but they are sufficiently suppressed to give a good estimate of the effect of removing these contributions.

4. Modified rates

We demonstrate the effect of suppressing large transverse momentum emissions by showing the ratio of the rate including the suppressing envelope and the original AMY rate in Fig. 13 as a function of k, the absolute value of the three-momentum of the emitted gluon.

For a typical α_s of 0.3, the suppression at small k is significant but decreases for larger k. As expected, the effect is also reduced as α_s decreases, as can be seen in the result for $\alpha_s = 0.01$.

5. Comparison AMY, BDMPS–Z, ASW–MS in a brick

Figure 14 compares the gluon emission spectra for AMY, BDMPS–Z and ASW–MS for two path lengths ($L = 2$ and 5 fm) and $T = 300$ MeV. In the AMY formalism the transport coefficient $\hat{q}$, which is used to set the medium density in the BDMPS–Z and ASW–MS calculations, is a derived quantity not a parameter to be set. For this comparison $\hat{q}$ was calculated using the $q \ll T$ limit of the HTL scattering rate (Eq. (16), with $q_{\max}^2 = ET$, so that $\hat{q} = 6\alpha_s T\mu^2 \ln(\sqrt{ET/\mu^2}))$).

The AMY curve (green line in Fig 14) is obtained by multiplying the rate $d\Gamma/dk$ Eq. 19 by the medium length L to obtain a radiation spectrum dN/dk. The curve labeled BDMPS–Z (black dashed) was calculated using Eq. 30, while the 'BDMPS–Z (low-x)' curve (solid black) was obtained using in addition the small-x approximation $xP_{q\to q}(x) \approx 2$ and $\omega_0 = -iC_A\hat{\hat{q}}/xp$. Comparing first the AMY curves with the BDMPS–Z curve in Fig. 14, one sees that the results are similar for $L = 5$ fm, while for short path lengths ($L = 2$ fm), AMY generates more radiation. This is due to the fact that AMY uses the limit $L \to \infty$ which ignores the increased effect of finite formation times at small length [73]. The ASW–MS calculation (blue curve in Fig. 14) is based on the BDMPS–Z formalism, but takes into account finite-length effects. These effects include vacuuum-medium interference effects, the formation time effect at small L and the large-angle cut-off $k < k_\perp$, although these aspects are not easily separated in the calculation [53]. The effect of the finite-length corrections is a pronounced reduction of the radiation at small gluon energies k, which is probably mostly due to the large angle cut-off.

The green dashed curve shows the AMY result with the large-angle cut-off described in the previous section. This reduces the radiation at small k, as expected, but the reduction is not as pronounced as in the ASW–MS calculation (compared to BMDPS–Z). The smaller effect of the cut-off in AMY is likely due to the softer, Gaussian, cut-off that is used in AMY, compared to a hard cut-off $k_\perp < k$ in ASW–MS, although it is not excluded that the transverse momentum spectra are different, which would also affect the cut-off. The dip in the AMY result around $k = E$ is caused by the cutoff (37) for the case that a gluon with momentum $k \sim p$ is radiated. In that

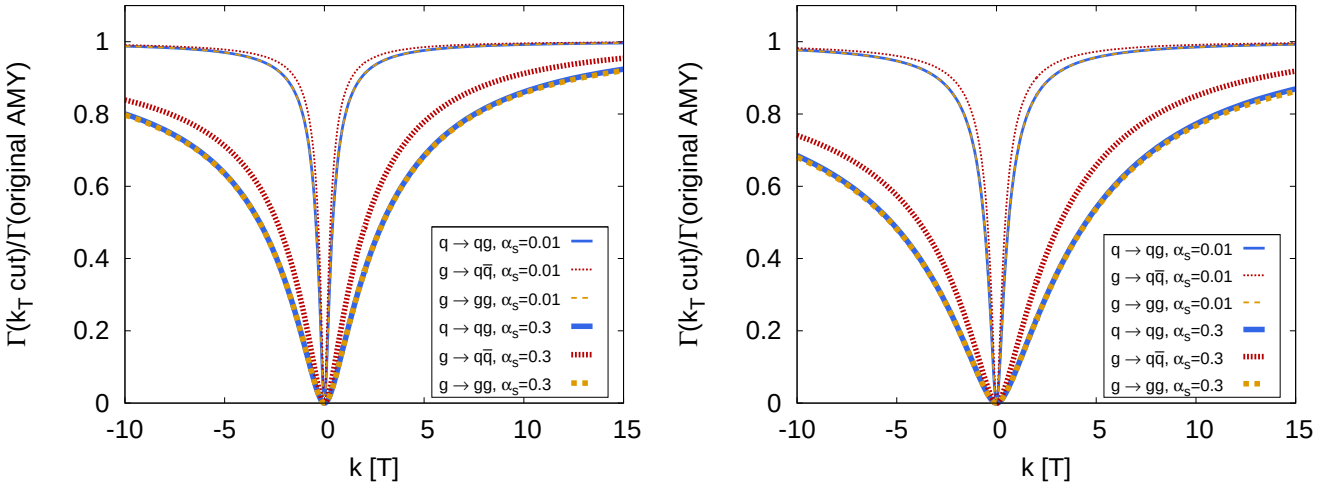


FIG. 13: (Color online) Ratio of the rate for the process $q \to qg$ suppressing emission angles larger than $\pi/2$ (left panel) and $\pi/4$ (right panel) and the original AMY rate for two different α_s and $p = 40\,T$. The lines for $g \to gg$ and $q \to qg$ coincide.

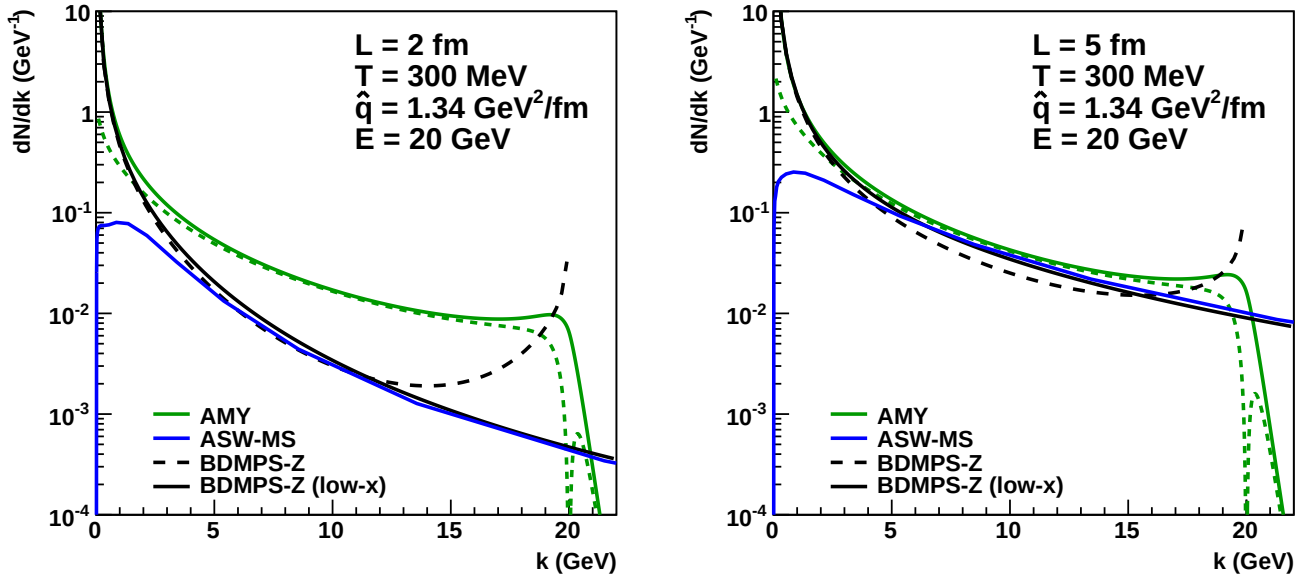


FIG. 14: (Color online) Gluon radiation spectra as a function of gluon momentum k for AMY (with and without $k_\perp$, max cut-off), ASW–MS, and the BDMPS–Z multiple soft scattering result Eq. 30 (with and without small x approximation) for a medium of length $L = 2$ fm (left panel) and $L = 5$ fm (right panel).

case the outgoing quark's longitudinal momentum $p - k$ is very small and even a small k_T can lead to a large angle for the outgoing quark. Hence, the cutoff becomes relevant and suppresses the rate in this case as it does for small outgoing gluon momentum.

D. The Higher-Twist (HT) approach

In the application of perturbative QCD to hard processes, a fundamental role is played by the so called factorization theorems [21]. These theorems demonstrate that all higher order corrections to a particular hard process may be cast in a form where the hard, short-distance part of a particular process can be separated order-by-order in coupling from the long-distance, soft parts of the process as long as one ignores terms which are suppressed

by powers of the hard scale of the process (generically denoted as Q^2). In the case of the simplest hard process: The total cross section in the deep-inelastic scattering (DIS) of an electron on a proton, these power corrections can be expressed in the simpler language of the Operator Product Expansion (OPE). In the OPE, the singular product of operators at closely separated points can be expressed as a series of terms which contain the product of progressively more complicated local operators and progressively less singular c-functions. The power suppression (i.e. power of Q^2 in the denominator) of each term depends on the "twist" of the local operator defined as the difference of the energy dimensions of the operator and the highest spin that can be constructed through the product of the various individual operators in the local product.

So far, factorization has been rigorously proven for the leading twist part of a set of high Q^2 processes such as single hadron inclusive e^+e^- annihilation, Drell-Yan, DIS, hadron-hadron collisions etc. Factorization at next-to-leading twist has been proved for a sub-class of processes, such as the total cross section in DIS [74]. As a result, there now exists a formulation of a class of higher twist corrections to the total cross section in DIS [75]. The higher twist energy loss approach is based on applying this formalism to the problem of calculating the change in the fragmentation function of a quark produced by the DIS of an electron on a nucleus [49, 76]. While the initial attempt focused on computing solely the single scattering correction to the one gluon emission cross section, this has been subsequently generalized to include both multiple emissions in a DGLAP like formalism [50], as well as multiple scattering [77]. In the following we will describe the pertinent details of the HT approach assuming that a quark is produced in a hard collision at one edge of the QGP brick. We will first describe the setup where a quark is produced in the DIS of an electron on a nucleus and then having factorized the initial state and hard cross section from the final state evolution of the produced quark, we will consider the change in the evolution of this quark as it moves through the brick.

1. *Gluon emission formalism*

In this section, we describe the radiative part of the higher-twist (HT) calculation as applied to the "brick problem". In short, the higher-twist calculation consists of including a class of medium corrections to the process of jet evolution in vacuum, brought about by the multiple scattering of the hard partons in a medium. It is most straightforwardly derived in the case of single inclusive deep-inelastic scattering in a large nucleus, with the nucleus playing the role of the medium. While most scattering corrections are suppressed by powers of the hard scale Q^2, a subset of these are enhanced by the length of the medium and these are included in the calculation. Thus, the expansion parameter in the HT approach is $\alpha_s \hat{q} L/Q^2$ where $\hat{q}$ is the transverse momentum squared imparted to a single parton per unit length and L is the length traversed by the parton.

Consider the case of deep inelastic scattering (DIS) on a nucleus (in the Breit frame). The nucleus has a large momentum in the positive light cone direction $A[p^+, 0, 0, 0]$ with p^+ the mean momentum of a nucleon. The incoming virtual photon has a momentum which may in general be expressed as $[-Q^2/2q^-, q^-, 0, 0]$; in the Breit frame $q^- = Q/\sqrt{2}$ (light-cone coordinates in this section use the convention $p^+ = \frac{1}{\sqrt{2}}(p^0 + p^3)$ and $p^- = \frac{1}{\sqrt{2}}(p^0 - p^3)$). The inclusive cross section to produce a hard hadron, which carries a momentum fraction z of the initial produced hard quark may be expressed in a factorized form as

$$\frac{d\sigma}{dz} = \int dx G(x, Q^2) \frac{d\hat{\sigma}}{dQ^2} D(z, Q^2), \tag{38}$$

where $G(x)$ is the parton distribution function (PDF) to obtain a hard quark in the nucleon with momentum fraction x. In the Breit frame the momentum of the incoming quark is $xp^+ = Q/\sqrt{2}$. Thus the produced quark has an outgoing momentum $q^- = Q/\sqrt{2}$. The produced quark is virtual with a virtuality smaller than the hard scale usually denoted as λQ where $\lambda \ll 1$. The other two factors are the hard partonic cross section $d\hat{\sigma}/dQ^2$ and the final fragmentation function $D(z, Q^2)$. The scale in the fragmentation function is the factorization scale and also represents the maximum possible virtuality of the produced hard jet. The fragmentation function at the scale Q may be obtained from a measured fragmentation function at a lower scale using the DGLAP evolution equations

$$\frac{\partial D_q^h(z, Q^2)}{\partial \log(Q^2)} = \frac{\alpha_S(Q^2)}{2\pi} \int_z^1 \frac{dy}{y} P_{q\to i}(y) D_i^h\left(\frac{z}{y}, Q^2\right). \tag{39}$$

There is an implied sum over flavors i which includes all possible types of partons that may split off from the hard leading quark denoted as q. The kinematics of the scattering and emission process may be illustrated with the diagram in Fig. 15.

In the case of DIS on a large nucleus, the above factorized form may be assumed to hold with the only change being the replacement of the vacuum evolved fragmentation function with a medium modified fragmentation function (as well as a replacement of the nucleon PDF with a nuclear PDF). The medium modified fragmentation function contains the usual vacuum evolution piece Eq. (39) and a medium piece which includes both terms which are interferences between medium induced radiation and vacuum radiation as well as terms where both the amplitude and the complex conjugate represent medium induced radiation. Once so factorized, the medium modified fragmentation function can be used to compute the single hadron inclusive cross section in any process by simply replacing the initial state parton dis-

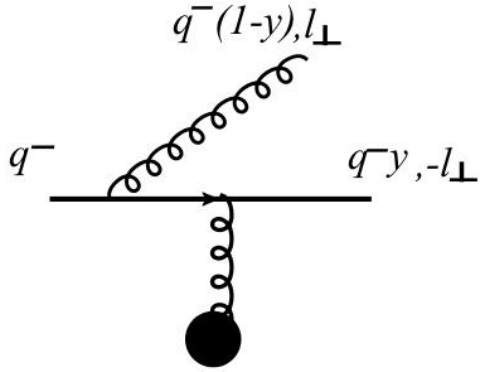


FIG. 15: A scattering and emission diagram with the corresponding momenta, using the notation convention of the Higher Twist formalism.

tribution and hard cross section by those appropriate for the process in question.

For the Brick Challenge we ignore all the initial state functions and hard cross sections. We assume that the quark is produced at one edge of the brick designated as the origin and travels in the negative light cone direction with a negative light cone momentum q^-. We assign the quark an initial virtuality Q^2. Since this is not the Breit frame in DIS there is no implied relation between q^- and Q^2. The equation for the medium modified fragmentation function with an initial light-cone momentum q^- and virtuality Q^2, which starts at the location ζ_i^- and exits at ζ_f^-, is given as

$$\frac{\partial D_q^h(z,Q^2,q^-)|_{\zeta_i}^{\zeta_f}}{\partial \log(Q^2)} = \frac{\alpha_S}{2\pi}\int_z^1 \frac{dy}{y}\int_{\zeta_i}^{\zeta_f} d\zeta P(y) K_{q^-,Q^2}(y,\zeta) D_q^h\left(\frac{z}{y},Q^2,q^- y\right)\Big|_{\zeta}^{\zeta_f}. \tag{40}$$

In the equation above, we have dropped the light-cone $(-)$ superscript on the positions. Note that the medium modified fragmentation function is now not only a function of Q^2 and z but also of q^- and ζ. The calculation of the evolution equation then requires the evolution of a three dimensional matrix (in z, q^-, ζ). The medium kernel $K_{q^-,Q^2}(y,\zeta)$ for a quark jet is given as [77]

$$K_{q^-,Q^2}(y,\zeta) = \frac{\left(\hat{q}(\zeta) - (1-y)\frac{\hat{q}}{2} + (1-y)^2\hat{q}_Q\right)}{Q^2}\left[2 - 2\cos\left(\frac{Q^2(\zeta-\zeta_i)}{2q^- y(1-y)}\right)\right]. \tag{41}$$

In the equation above, $\hat{q}(\zeta)$ without any subscripts represents the position (ζ) dependent transport coefficient of a gluon, which may be expressed in operator form as

$$\hat{q} = \frac{8\pi^2\alpha_s C_A}{N_c^2-1}\int dy^- \langle X|Tr\left[F^{a\mu\nu}(y^-)v_\mu F^{a\sigma}_\nu v_\sigma\right]|X\rangle \tag{42}$$

where, $F^{a\mu\nu}$ is the position dependent field strength tensor of the gluon field and y^- represents the light-cone separation between these two field insertions. The state $|X\rangle$ represents the matter through which the jet propagates. We note that in the evaluation of multiple scattering diagrams leading to Eq. 41, it is assumed that the transverse momentum exchanged with the medium $\vec{k}_\perp$ is soft, so that a Taylor expansion can be made. The leading non-zero term in this expansion is the term proportional to the square i.e. $|\vec{k}_\perp|^2$. In combination with the gluon vector potential this term yields the transport coefficient $\hat{q}$. The effect of higher terms in the Taylor expansion of $\vec{k}_\perp$ is ignored, so that distribution of $\vec{k}_\perp$ is approximated as a two-dimensional Gaussian with a mean $\vec{k}_\perp = 0$ and a width proportional to $\hat{q}$.

The $\hat{q}$ for a quark scattering off the gluon field is related to the above expression as $\hat{q}_Q = \frac{C_F}{C_A}\hat{q}$. In the factorized formalism of the HT approach, there is no scheme to evaluate these coefficients and thus their values are external to the formalism. In most cases these are taken as fit parameters which are dialed to match one data point.

2. *Single gluon emission*

A gluon emission spectrum dN/dz can be calculated by integrating Eq. 40 over Q^2 using the gluon radiation kernel Eq. 41 and the gluon momentum fraction $z = (1-y)$, giving

$$\frac{dN}{dz} = C_F\frac{\alpha_S}{2\pi}\frac{1+(1-z)^2}{z}\int_{Q^2_{\min}}^{Q^2_{\max}}\frac{dQ^2}{Q^2}\int_0^L d\zeta\frac{\hat{q}(\zeta)}{Q^2}\left[2-2\cos\left(\frac{Q^2\zeta}{2Ez(1-z)}\right)\right] \tag{43}$$

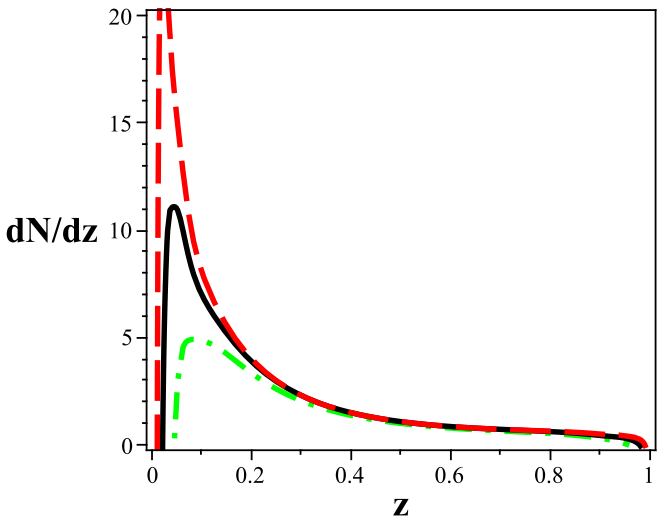


FIG. 16: The single gluon emission kernel in the HT approach for a quark with energy $E = 20$ GeV in a static medium of length 4 fm which has a $\hat{q}_Q = 1$ GeV^2/fm with the maximum momentum cutoff from the medium set at $M = 1.2$ GeV (black solid line). The variable z here is equivalent to the variable x^+ used in the WHDG approach, earlier in this paper. Also shown are the single gluon spectra for $M = 2.4$ GeV (red dashed line) and $M = 0.6$ GeV (green dot-dashed line). See text for details.

where we have taken only the first term of the emission kernel, and ignored terms which are suppressed by factors $z = (1 - y)$ (soft gluon approximation). The lower bound for the Q^2 integral is given by the requirement that the formation time of the gluon should be smaller than the length of the medium: $Q^2_{\rm min} = E/L$. The upper integration limit is given by

$$Q^2_{\rm max} = y(1-y)2q^-p^+ = z(1-z)2ME, \qquad (44)$$

which is discussed further below (cf. Eq. 45).

The medium induced single gluon emission distribution in momentum fraction z is plotted in Fig. 16, for a 20 GeV quark, propagating through a 4 fm long static brick, using $M = 3T$.

The medium induced gluon emission kernel has soft divergences at $y = 0, 1$ as is the case for the gluon emission kernel in vacuum. However, given that $\hat{q}$ is very similar to a gluon distribution function it depends on the momentum fraction of the gluon off which the hard parton scatters. In the case of DIS, this momentum fraction, referred to as x_L, is given as $x_L = Q^2/(2q^-p^+y(1-y))$. Where, $p^+ = M/\sqrt{2}$, M is the mass of the nucleon and $q^- = \sqrt{2}E$, where E is the energy of the virtual photon in the nucleus rest frame. One expects $\hat{q}(x_L)$ to be dominated by small values of the fraction x_L and rapidly vanish for values of $x_L > 1$. This introduces a constraint on the radiated gluon momentum fraction,

$$\frac{1}{2} - \sqrt{\frac{1}{4} - \frac{Q^2}{2q^-p^+}} < y < \frac{1}{2} + \sqrt{\frac{1}{4} - \frac{Q^2}{2q^-p^+}}. \qquad (45)$$

Note that in the above equation $Q^2 \simeq k^2_\perp$ the transverse momentum of the radiated gluon. Since only values of y which lie between 0 and 1 are allowed, the value of $k^2_\perp$ is always constrained to be less than q^-p^+ where p^+ is the momentum of the proton. In a multiple scattering scenario, this constraint only applies to the largest $k_\perp$, i.e. the first emission. Successive emissions are ordered in $k_\perp$. While, this limit is well defined in DIS, it is slightly uncertain in the case of a quark gluon plasma created in a heavy-ion collision. However, one argues that the probability of a medium at a temperature T to radiate a gluon with momentum much larger than the mean momentum of $3T$ should be very small. Thus one replaces $p^+ = M/\sqrt{2} \to 3T/\sqrt{2}$ in the equation above. Here, M represents the largest momentum that may be exchanged between the medium and the jet, which is achieved when a thermal parton from the medium directly impacts with the jet. The central black solid line in Fig. 16 corresponds to the choice of $T = 400$ MeV, with $M = 3T = 1.2$ GeV. The red dashed line corresponds to the replacing the upper limit with $M = 6T = 2.4$ GeV and the dot-dashed green line to replacing the upper limit with $M = 3T/2 = 0.6$ GeV. We note that the main difference occurs at at low z, i.e. in the soft gluon limit, as would be expected

3. *Multiple gluon emission*

We now plot the result of multiple emissions from the single quark parton produced at one edge of a static brick. In the soft gluon limit, the medium modified fragmentation function of a quark is obtained by replacing the vacuum splitting function with the sum of the vacuum splitting function and the medium modified splitting function in Eq. (40). These equations require an input fragmentation function at some lower initial scale usually chosen to be 1 GeV. The input fragmentation function is usually chosen to be the vacuum fragmentation function. Note that even if the initial input fragmentation function is assumed to have no position dependence, the evolution equation generates a position dependence in the evolved fragmentation functions at any higher scale. A more correct input is to have a position dependent fragmentation function which is the vacuum fragmentation function at distances beyond the brick and goes to zero swiftly for fragmentation within the brick. For the HT plots in this paper we will ignore this sophistication and ignore the position dependence of the fragmentation function. Even at this level of approximation, the equations above are far too numerically intensive to solve. One usually replaces the position dependence with the initial position $\zeta \to \zeta_i$. The evolution equations now represent the evolution of

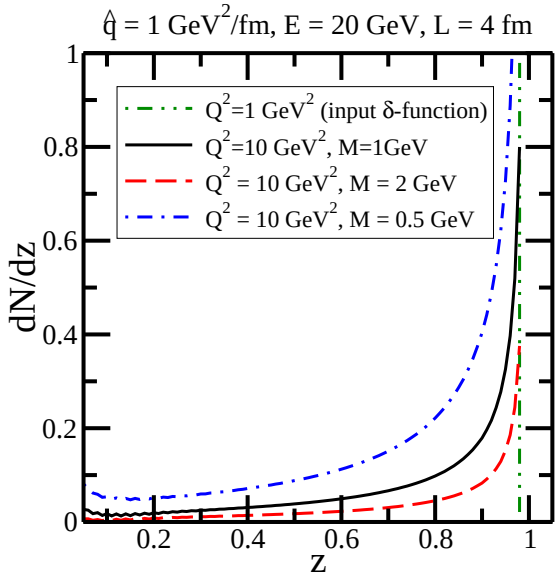


FIG. 17: The results of evolving an input $[q(\bar{q}) \to q(\bar{q})]$ fragmentation function at $\mu^2 = 1$ GeV^2 given by a $\delta(1-z)$ (see Eq. (46)) up to a higher scale of $Q^2 = 10$ GeV^2 in a 4 fm brick. The transport coefficient $\hat{q}_Q = 1$ GeV^2/fm with the maximum momentum cutoff from the medium set at 1 GeV (solid black line), 2 GeV (red dashed line) and 0.5 GeV (blue dash-dotted line). See text for details.

a two dimensional matrix and these represent the calculations which will be presented in this paper. A further approximation which is sometimes used in the literature is to also drop the energy dependence of the fragmentation functions. This approximation will not be made and the energy dependence of the medium modified fragmentation function will be retained.

In order to compare with other formalisms which present the energy loss of a single quark, we introduce a quark-to-quark fragmentation function as the input at the lower scale of $\mu^2 = 1$ GeV^2. In actuality our input is a singlet quark fragmentation function ($(q+\bar{q})/2 \to (q+\bar{q})/2$). Our input at 1 GeV may be expressed as

$$\begin{aligned} D_{\frac{u+\bar{u}}{2}\to\frac{u+\bar{u}}{2}}(z, 1\text{GeV}^2) &= \delta(1-z) \\ D_{\frac{d+\bar{d}}{2}\to\frac{u+\bar{u}}{2}}(z, 1\text{GeV}^2) &= 0 \\ D_{g\to\frac{u+\bar{u}}{2}}(z, 1\text{GeV}^2) &= 0. \end{aligned} \tag{46}$$

In Fig. 17, these are represented by the solid green line $[u(\bar{u}) \to u(\bar{u})]$ along the $z = 1$ axis and the cyan dot-dashed line $[g \to u(\bar{u})]$ along the $dN/dz = 0$ axis. We do not plot the results of the $d(\bar{d}) \to u(\bar{u})$ fragmentation. These distributions are then evolved up to the higher scale of $Q^2 = 10$ GeV^2. The results for the three different momentum bounds from the medium $M = 1.5T$, $3T$ and $6T$ (as discussed above) with $T = 1/3$ GeV and a quark $\hat{q}_Q = 1$ GeV^2/fm are plotted in Fig. 17. Note that the full quark and gluon distributions are evolved. This means that if in one step of the evolution a hard quark loses energy by splitting into a quark and a gluon, in the next step of the evolution both the softer quark and gluon will further lose energy by splitting themselves.

As would be expected, we note that in the case when the bound from the medium is set at the higher value of $M = 2$ GeV, there is more gluon radiation and thus there is more modification of the input distribution and vice-versa for the case when the bound is set at a lower value of $M = 0.5$ GeV. The dependence of the evolved distribution on the bound is enhanced primarily due to the numerical instability of the vacuum DGLAP evolution equations on an input distribution that is singular at $z \to 1$. Note that the evolution equations include a pure vacuum part and a medium induced part as expressed in Eq. (40). The pure vacuum splitting functions are defined using the (+)-functions, i.e.,

$$\begin{aligned} \frac{\partial D(z,Q^2)}{\partial \log Q^2} &= \frac{\alpha^2}{2\pi}\int_z^1 \frac{dy}{y} P(y)_+ D\left(\frac{z}{y}, Q^2\right) \\ &= \frac{\alpha^2}{2\pi}\int_z^1 \frac{dy}{y} P(y) D\left(\frac{z}{y}, Q^2\right) - D(z,Q^2)\int_0^1 dy P(y). \end{aligned} \tag{47}$$

The above equation assumes that $D(z)$ is well defined at all values of z over which the evolution is carried out. This condition is not fulfilled by the strict δ-function. The calculations presented in Fig. 17 are carried out by using a regulator to define the δ-function. We should point out that only one choice of regulator has yielded convergent results as the regulator is removed from the results, viz.

$$\begin{aligned} \delta(1-z) &= \frac{1}{\epsilon}, \quad \forall \quad z > 1-\epsilon, \\ &= 0, \quad \forall \quad z < 1-\epsilon, \end{aligned} \tag{48}$$

in the limit $\epsilon \to 0$. Other choices of regulation, e.g. a narrow Gaussian with a width given by ϵ turned out to yield results which were non-convergent within the limits of numerical accuracy used.

4. *Medium modified fragmentation function*

The DGLAP evolution equations used by the HT scheme require that the input fragmentation function be well defined at all values of momentum fraction z. To illustrate the degree of control in these calculations we now repeat the calculation above but using a well defined input distribution: a π^0 fragmentation function (in this case taken from the KKP parametrization [78]). The input is taken at $\mu^2 = 1$ GeV^2 and evolved to 10 GeV^2. The results are plotted in Fig. 18 The brick is again of length 4 fm and has a quark $\hat{q}_Q = 1$ GeV^2/fm. Since fragmentation functions vary over orders of magnitude as z runs from 0 to 1 we plot the ratio of the medium modified fragmentation function to a vacuum fragmentation function at the same scale. The denominator is obtained by evolving the fragmentation function from 1

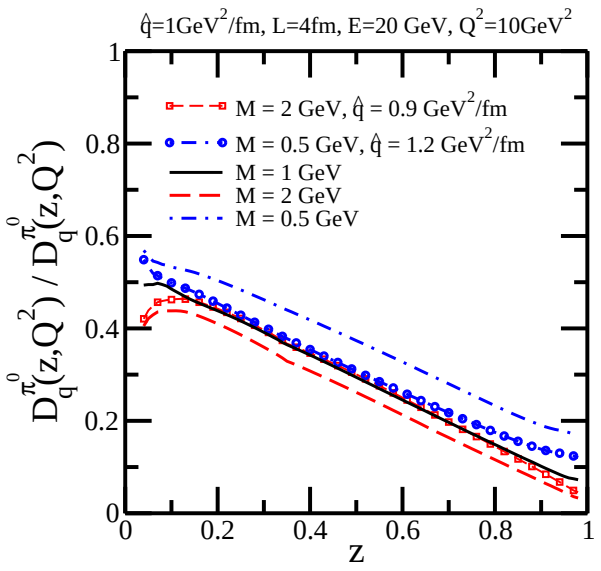


FIG. 18: The ratio of the medium modified fragmentation function (of a π^0 from a quark with $E = 20$ GeV) to the vacuum fragmentation function at $Q^2 = 10$ GeV^2. The input in both cases is the KKP fragmentation function at $\mu^2 = 1$ GeV^2. The medium is a static brick with a length of 4 fm and a $\hat{q}_Q = 1$ GeV^2/fm. Three different values for the maximum momentum cutoff from the medium are used 1 GeV (black solid line), 2 GeV (red dashed line), and 0.5 GeV (blue dot-dashed line). The open red squares and open blue circles indicate the results with $\hat{q}_Q$ changed to make the lines with $M = 2$ GeV and $M = 0.5$ GeV approximately coincide with the central line with $M = 1$ GeV. See text for details.

GeV^2 to 10 GeV^2 with a $\hat{q}_Q = 0$. The black solid line represents the standard case with a bound on the momentum from the medium set at $M = 1$GeV. The red dashed and the blue dot-dashed lines represent the cases with $M = 2$ GeV and $M = 0.5$ GeV. As expected, raising the bound, increases the phase space of gluon radiation and thus increases the modification.

5. *Uncertainty due to large angle radiation*

The uncertainty in the bound on the momentum that may emanate from the medium introduces an uncertainty in the extracted value of $\hat{q}$. To estimate this uncertainty, we take the case with $M = 0.5$ GeV (the blue dot-dashed) which shows less modification than the case with $M = 1$ GeV and increase the $\hat{q}$ until the blue dot-dashed line coincides with the black line. The final result is indicated with a blue dot-dashed line with open circles. This requires a 30% increase in $\hat{q}_Q$. Similarly we reduce the $\hat{q}_Q$ for the case with $M = 2$ GeV (red dashed line) to make it coincide with the black line. The final result is indicated by the red dashed line with open squares and requires a $\hat{q}_Q$ which is 10% lower than the central value of 1 GeV^2/fm. Thus the uncertainty in the extracted value of $\hat{q}$ in HT calculations is between 10% to 30% when the $\hat{q}_Q \sim 1$ GeV^2/fm and the length of the medium is of the order of 4 fm. The reader will note that these values are quite representative of the respective values at RHIC and thus provide the range of error in estimates of $\hat{q}$ extracted in RHIC collisions.

IV. SYSTEMATIC COMPARISONS

In this section, the multiple-soft scattering approximation is compared with the opacity expansion formalism and the McGill AMY implementation. Specifically, the following energy loss models are compared:

- ASW–MS: The multiple-soft scattering approximation as formulated by ASW [39] and discussed in Sections III A and III C.
- ASW-SH: The single hard scattering approximation as described formulated by ASW [39], and shown in Eq. (3 and Table I. The original formulation uses a fixed value for $L/\lambda = 1$ for analytical convenience. For this work L/λ is calculated from the temperature T in the medium (see Appendix A).
- DGLV: The single hard scattering approximation using the same choices for in-medium gluon and quark masses and the kinematic bounds as used by WHDG [47], as given in Eq. 2 and Table I.
- AMY radiative: The AMY formalism based on a thermal effective field theory as described in Section III C. In the interest of the comparison to the other formalisms, the gluon splitting process $g \to gg$ is removed from the calculation.

A. Comparison at fixed temperature

Figure 20 shows the single gluon energy spectra for medium-induced radiation for a uniform medium with $T = 300$ MeV and two different path lengths $L = 2$ fm (left panel) and $L = 5$ fm (right panel) using the four different formalisms discussed above. The HTL-based AMY formalism (green curve) used here is without the large-angle cut-off discussed in Section III C 3 and it gives the largest amount of radiation. The opacity expansions (red curves, DGLV and ASW–SH) and the Higher Twist formalism (black curves, HT) are next while the multiple-soft scattering approximation ASW–MS gives the least radiation. For ASW–MS and HT two curves are shown, using different relations between the transport coefficient $\hat{q}$ and the temperature T. One is based on the soft-scattering limit from HTL field theory, Eq. 16, which gives $\hat{q} = 2\,C_A\,\alpha_s\,T\,\mu^2\,\log(q^2_{\rm max}/\mu^2))$ while the other is Eq. A6, based on Eq. A5. The single gluon spectrum for the HT formalism is evaluated using Eq. 43 which

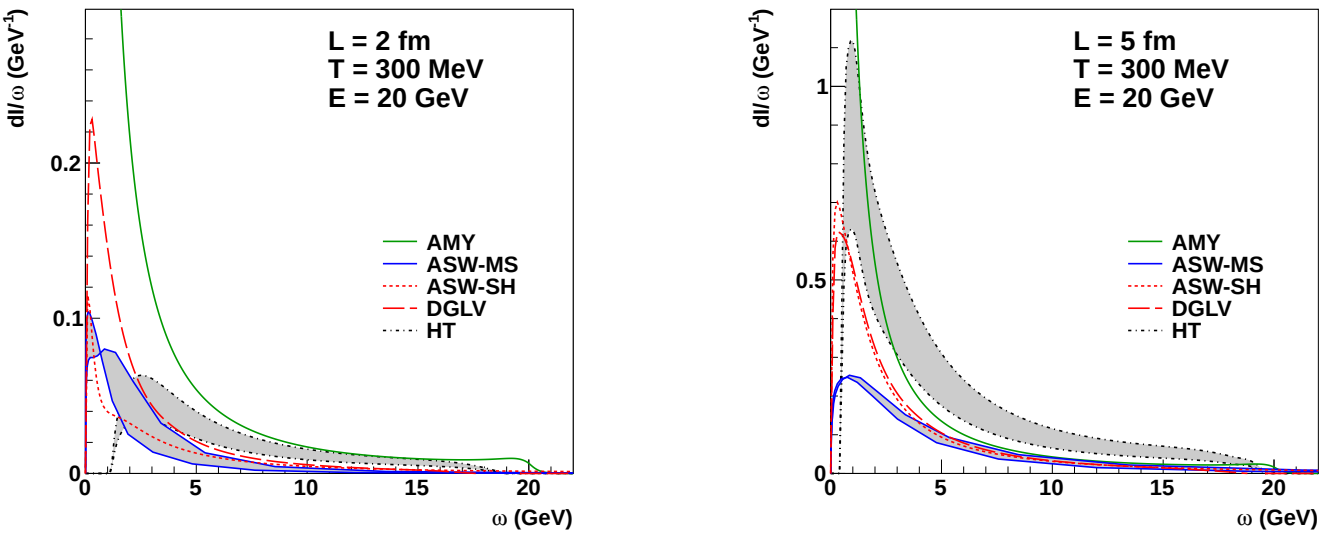


FIG. 19: (Color online) The single gluon distribution as function of gluon energy ω for a uniform medium with $T = 300$ MeV and two different lengths, $L = 2$ fm (left panel) and $L = 5$ fm (right panel). For the AMY calculation, the outgoing gluon spectra are plotted, including the evolution via the rate equation Eq. 21. The bands for the ASW–MS and HT formalisms indicate the uncertainty from evaluating $\hat{q}$ using Eq. 16 and A6.

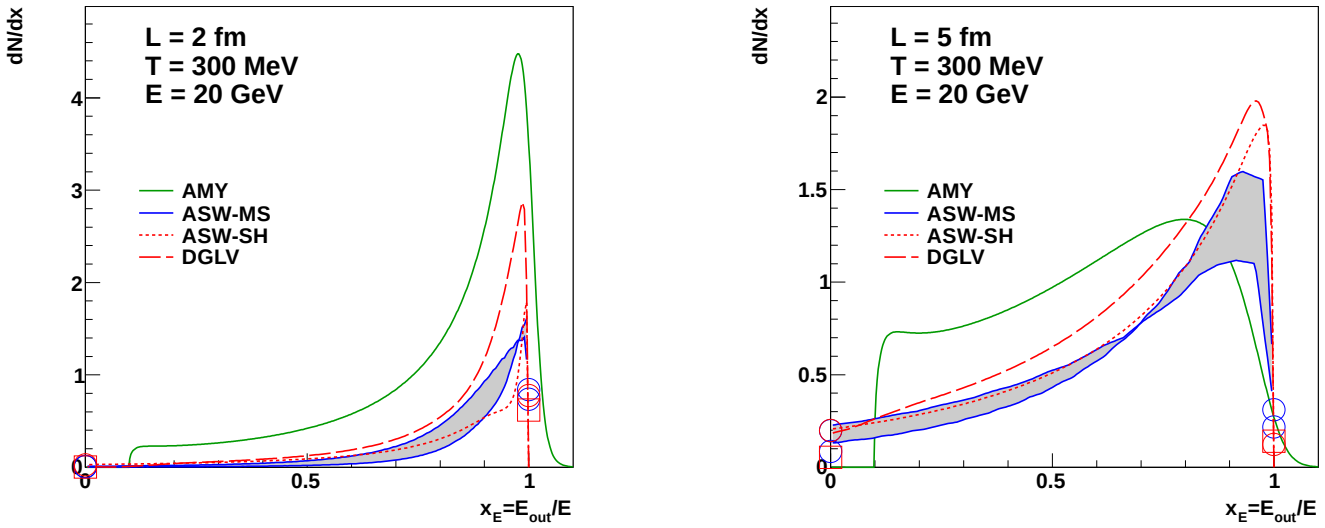


FIG. 20: (Color online) The final quark energy spectrum as function of $x_E = E_{out}/E = 1 - \epsilon$ for a uniform medium with temperature $T = 300$ MeV and two path lengths $L = 2$ fm (left panel) and $L = 5$ fm (right panel). The symbols at $x_E = 0$ indicate the probability that a quark is absorbed and at $x_E = 1$ the probability that a quark does not interact with the medium. Blue circles: ASW–MS. Open red squares: DGLV. red circles: ASW–SH.

does not include modified DGLAP-evolution of the partons. The HT formalism gives more radiation at larger gluon energies than the opacity expansion and ASW–MS, while the peak at small ω is less pronounced for the default $Q^2_{\rm max} = 6z(1-z)ET$. See Fig. 16 to see the effect of changing $Q^2_{\rm max}$. We also note that the $L = 5$ fm case is beyond the strict validity of the HT formalism, since the lower virtuality bound $Q^2_{\rm min} = E/L \approx 0.4$ GeV^2. Despite this, the result is shown for comparison.

A similar ordering between the different formalisms is visible for $L = 2$ fm and $L = 5$ fm, although the difference between the AMY result and the opacity expansions is larger at small L. The peak at small ω for the HT formalism is also more pronounced for larger path length. The path-length dependence has been studied in more detail in [56], where is is shown that for small L, AMY

overestimates the radiation by ignoring finite-length effects, while for large path-lengths, the first order ($N = 1$) opacity expansion overestimates the radiation by neglecting interference between subsequent scatterings. At large path-lengths, the AMY result is close to the ASW–MS result, but only for large gluon energies. At smaller gluon energies, the large-angle cut-off strongly reduces radiation in ASW–MS. This effect is not implemented in AMY (see Section III C 3).

For ASW–MS and ASW–SH the thermal quark and gluon masses are set to zero while in DGLV those masses are finite. Including the thermal masses reduces soft gluon radiation which can be seen comparing the ASW–SH and DGLV curves at small ω. Another difference as discussed in Section III B is the cut-off $k_{\max}$ on the transverse momentum of the radiated gluon. For ASW–MS and ASW–SH it is possible that a radiated gluon has larger momentum than the initial energy of the incoming quark because there is no kinematical bound on the gluon energy ω.

To calculate the total energy loss, the gluon spectra from Fig. 19 are used as input for a calculation of multiple gluon emission. For the opacity expansions and the ASW–MS calculation, a Poisson ansatz is used (Eq. 1), while AMY use rate equations (Eq 21). The resulting outgoing quark spectra are shown in Fig. 20. No results for the HT formalism are shown, because medium-induced and vacuum radiation cannot be separated in the medium-modified DGLAP evolution, which makes it difficult to compare to the other formalism on the same footing. The Poisson ansatz used for the opacity expansions and ASW–MS gives a finite probability to the parton to lose no energy (zero gluons radiated) which is indicated by the symbols at $x_{\rm E} = 1$ in Fig. 20. At the same medium density and $L = 5$ fm, this probability is approximate twice as large for the multiple soft scattering approximation as for the opacity expansions (right panel of Fig. 20). On the other hand, the gluons that are radiated are softer for the opacity expansions than for ASW–MS. For a brick of $L = 2$ fm and a temperature of $T = 300$ MeV the discrete weights at $x_{\rm E} = 1$ are between 0.5 and 1 (see also Table III), so that the behaviour is dominated by the discrete weights, although there are large probabilities for small energy loss $x_{\rm E} \gtrsim 0.8$ as well. The distribution from the AMY formalism is cut off at $x_{\rm E} < 0.1$, because the formalism is not valid when then parton energies approach the thermal energy; partons with energy less than 2 GeV are removed from the evolution.

It is clear from Fig. 20 that the different energy loss formalisms do not result in similar outgoing quark distributions.

B. Suppression factor in a QGP Brick

To characterise the energy loss distributions in Fig. 20 in a single number, we calculate an approximation of the nuclear suppression factor R_{AA} in the following way.

The measured hadron spectra at RHIC approximately follow a power law: $dN/dp_T = Ap_T^{-n}$. If the energy of each hadron is reduced by a fraction ϵ, the hadron momentum after energy loss $p'_T = (1-\epsilon)p_T$ and the spectrum after energy loss

$$\frac{dN}{dp'_T} = A\frac{(1-\epsilon)^n}{p_T^n}\frac{dp_T}{dp'_T} = A\frac{(1-\epsilon)^{n-1}}{p_T^n}. \qquad (49)$$

In this case $R_{AA} = (1-\epsilon)^{n-1}$. This can be generalized to a distribution of energy loss, in which case the nuclear modification factor R_{AA} can be approximated by the appropriately weighted average over the energy loss probability distribution $P(\epsilon)$

$$R_n = \int_0^1 d\epsilon (1-\epsilon)^{n-1} P(\epsilon), \qquad (50)$$

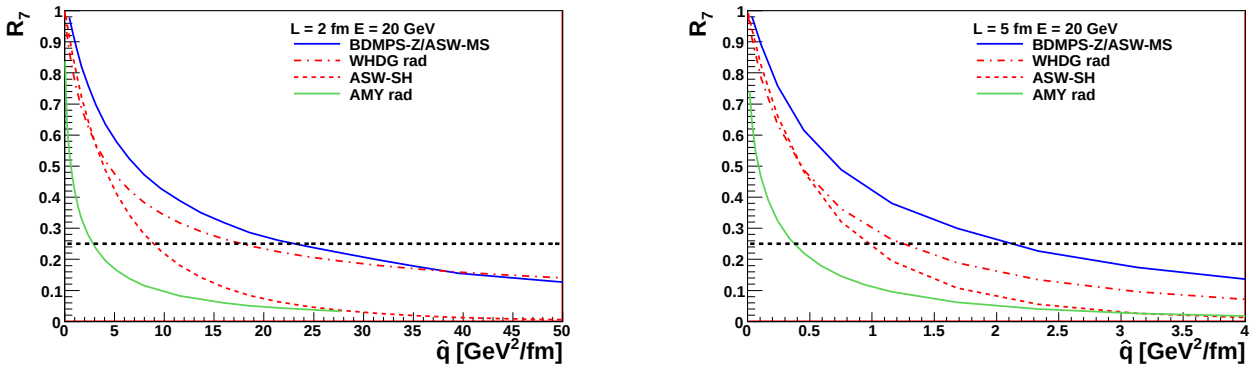
with $\epsilon = \Delta E/E$. In the following, R_7 will be used as a proxy for R_{AA}, because for RHIC energies the hadron p_T spectrum can be approximated by a power law spectrum with $n = 6.5$ for $p_T > 2$. GeV/c [79].

Figure 21 shows the dependence of the suppression factor R_7 on $\hat{q}$ for the different formalisms. The figure clearly shows that both opacity expansion formalisms generate a larger suppression at the same medium density (same $\hat{q}$) than the multiple soft scattering approximation. The AMY formalism generates the largest suppression at a given density. The values of the transport coefficient needed to reach a similar suppression as measured at RHIC [80–82], $R_7 \approx 0.25$, are listed in Table II and differ by a factor 5–10 between AMY and ASW–MS.

C. Comparison at fixed suppression R_7

In Fig. 22 the inclusive gluon spectra are shown for a uniform medium of $L = 2$ and 5 fm, for a fixed suppression $R_7 = 0.25$ using the medium density values given in Table II. The single gluon spectrum from DGLV does not extend beyond $\omega = E$ because that formalism implements a large momentum cut-off to impose forward propagation of the final state quark (cf. Eq. 11). For the AMY gluon spectrum only $q \to q + g$ splittings are included. In the AMY formalism it is not possible to distinguish between thermal and radiated gluons for $\omega < 2$ GeV which is why in this region for AMY the gluon spectrum is not shown. We note that the ASW–MS single gluon spectrum at fixed suppression is harder than that obtained in the opacity expansions.

Figure 23 shows the outgoing quark energy spectrum as function of $x_E = 1 - \epsilon$ for the two bricks of different lengths and $R_7 = 0.25$. The probability that a parton is absorbed in the medium is indicated by the markers at $x_{\rm E} = 0$. In this case the the energies of the multiple radiated gluons add up to a total energy loss that exceeds the initial energy of the parent parton and the parton is absorbed in the medium. The large x cut-off on the single



(a) $L = 2$ fm.

(b) $L = 5$ fm.

FIG. 21: Correlation between R_7 and $\hat{q}$ for a primary quark with $E = 20$ GeV for different energy loss formalisms. The horizontal black dashed line indicates $R_7 = 0.25$.

$R_7 = 0.25$		T (MeV)	$\hat{q}$ (GeV^2/fm)	ω_c or $\bar{\omega}_c L/\lambda$ (GeV)	R or $\bar{R}L/\lambda$	L/λ	m_D (GeV)
$L = 2$ fm	ASW–MS	1030	23.2	236	2393	—	—
	WHDG	936	17.8	105	1063	6.25	1.82
	ASW–SH	727	8.86	49.0	500	4.85	1.41
	AMY	480	2.7	—	—	—	—
$L = 5$ fm	ASW–MS	434	2.11	134	3401	—	—
	WHDG	358	1.23	36.5	925	5.97	0.69
	ASW–SH	326	0.95	27.6	702	5.44	0.63
	AMY	235	0.4	—	—	—	—

TABLE II: Values of the model parameters required to reach the typical suppression of $R_7 = 0.25$.

gluon spectra in the DGLV formalisms leads to a smaller probability for absorption than in ASW–MS and ASW–SH. The corresponding probability for losing no energy at all is given by the markers at $x_E = 1$.

The probabilities for absorption and no interaction of the multiple-soft scattering approximation are larger than for the opacity expansions. The continuous part of the energy loss probability distribution is more relevant in the opacity expansion than for the multiple soft scattering approximation.

In the AMY formalism, the outgoing quark spectrum peaks at $x_E = 0.9$, which corresponds to an energy loss $\Delta E \sim 2$ GeV. This radiation falls in the the region where we cannot distinguish the radiated gluons from the thermal gluons in the AMY formalism, as indicated by the cut in Fig. 22.

1. *Some characteristic quantities*

When all the models are tuned to a fixed amount of suppression R_7, the radiated gluon spectra are quite different. To quantify the difference, we calculate a few characteristic quantities for energy loss which are tabulated in Table III.

The average number of emitted gluons can be obtained by integrating the gluon spectrum (e.g. Fig. 22) over the gluon energy ω:

$$\langle N_g \rangle = \int d\omega \frac{dI}{d\omega}. \tag{51}$$

Note that this determines the probability for no energy loss:

$$p_0 = e^{-\langle N_g \rangle}. \tag{52}$$

The probability for complete absorption of the parton is given by

$$p_1 = \int_E^\infty d(\Delta E)\ P(\Delta E), \tag{53}$$

where E is the energy with which the parent parton enters the brick. The total average energy loss for the incoming parton is calculated from the energy loss probability distribution $P(\Delta E)$:

$$\langle \Delta E \rangle = \int_0^E d(\Delta E)\ P(\Delta E), \tag{54}$$

for which only the surviving partons are taken into account. For the AMY formalism the integral starts at

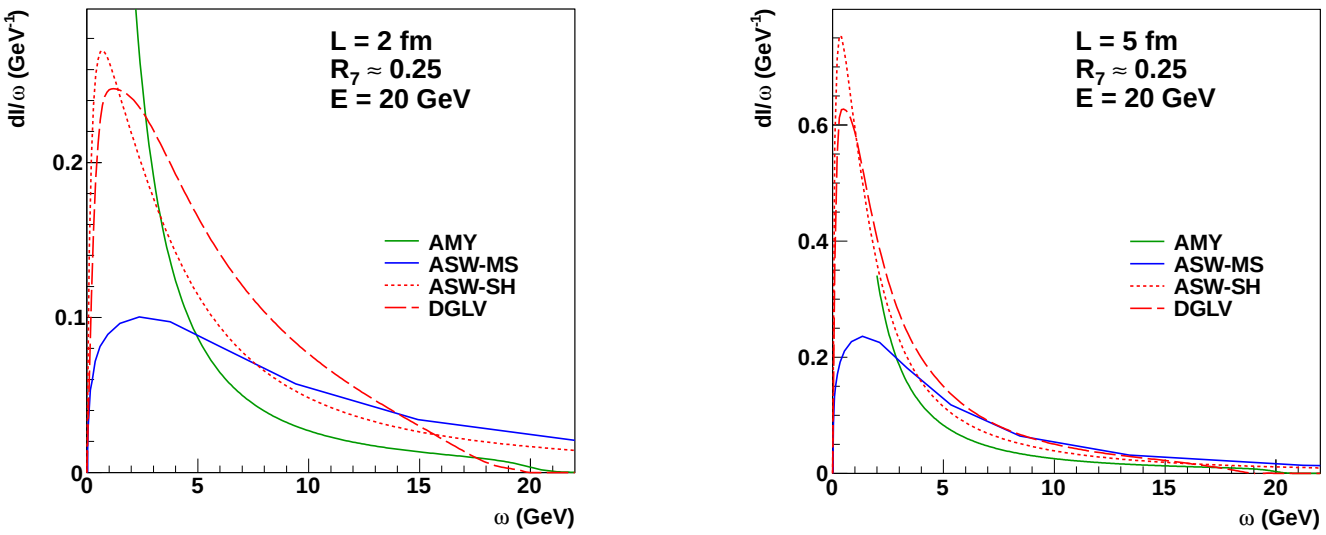


FIG. 22: Inclusive gluon radiation spectrum for quarks with $E = 20$ GeV with in-medium path-lengths $L = 2$ fm (left panel) and $L = 5$ fm (right panel). The medium density has been tuned for each formalism to give $R_7 = 0.25$. The AMY result includes the evolution via the rate equations Eq. 21.

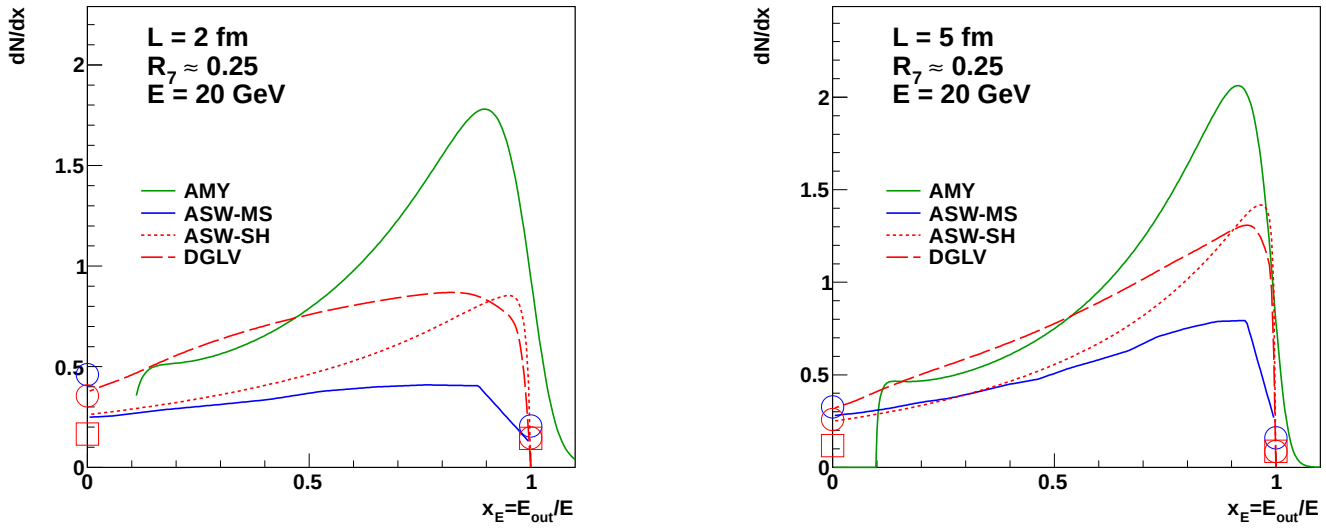


FIG. 23: The final quark energy spectra as function of $x_{\rm E} = 1 - \epsilon$ and for path-lengths $L = 2$ fm (left panel) and $L = 5$ fm (right panel). All models are scaled to the same suppression $R_7 = 0.25$. The squares at $x_{\rm E} = 0$ indicate the probability that a quark is absorbed and at $x_{\rm E} = 1$ the probability that a quark does not interact with the medium. Solid blue squares: BDMPS-Z/ASW–MS. Open red squares: DGLV. Solid red squares: ASW–SH.

negative energies (in principle $-\infty$) because the parton can also absorb energy from the medium (see Figs 20 and 23).

The values collected in Table III show that tuning the models to the same suppression factor R_7 does not imply that the mean energy loss is the same. On the other hand, when the suppression factor R_7 is fixed, the number of radiated gluons is similar.

V. CONCLUSION

For a summary of the main findings we refer back to Section II D.

		$T = 300$ MeV				$R_7 =$ 0.25			
		$\langle N_g \rangle$	$\langle \Delta E \rangle$ (GeV)	p_0	p_1	$\langle N_g \rangle$	$\langle \Delta E \rangle$ (GeV)	p_0	p_1
$L = 2$ fm	AMY		3.95				6.58		
	ASW–MS	0.17	0.3	0.84	0.01	1.58	5.9	0.2	0.46
	WHDG	0.48	1.24	0.62	0.00	1.94	7.7	0.14	0.14
	ASW–SH	0.25	0.93	0.78	0.03	1.92	6.9	0.15	0.35
$L = 5$ fm	AMY		8.30				6.47		
	ASW–MS	1.17	3.95	0.31	0.08	1.83	6.4	0.16	0.33
	WHDG	1.96	5.63	0.14	0.05	2.44	7.3	0.09	0.11
	ASW–SH	2.09	5.76	0.12	0.2	2.47	6.7	0.08	0.26

TABLE III: Table of different variables for the different energy loss models. Left columns: for $T = 300$ MeV for all models. Right columns: corresponding medium properties required to reach the typical suppression $R_7 = 0.25$.

Acknowledgements

The authors would like to acknowledge useful and interesting discussions with Peter Arnold, Steffen Bass, Ullrich Heinz, and Bronislav Zakharov. This research was financially supported by Ministerio de Ciencia e Innovacion of Spain (grants FPA2008-01177 and FPA2009-06867-E), Xunta de Galicia (Consellera de Educacion and grant PGIDIT10PXIB 206017PR), project Consolider-Ingenio 2010 CPAN (CSD2007-00042), FEDER, the Natural Sciences and Engineering Research Council of Canada, the Netherlands Organisation for Scientific Research (NWO), the US Department of Energy under DOE Contracts DE-FG02-05ER-41367, DE-SC0005396, DE-AC02-05CH11231, DE-AC02-98CH10886, DEAC-76-00098, DE-SC0004286 and (within the framework of the JET Collaboration) DE-SC0004104, and by a Lab Directed Research and Development Grant from Brookhaven Science Associates.

[1] K. Adcox et al. (PHENIX), Phys. Rev. Lett. **88**, 022301 (2002), nucl-ex/0109003
[2] C. Adler et al. (STAR), Phys. Rev. Lett. **89**, 202301 (2002), nucl-ex/0206011
[3] J. Adams et al. (STAR Collaboration), Phys.Rev.Lett. **91**, 072304 (2003), nucl-ex/0306024
[4] J. Adams et al. (STAR Collaboration), Phys.Rev.Lett. **97**, 162301 (2006), nucl-ex/0604018
[5] A. Adare et al. (The PHENIX Collaboration), Phys.Rev.Lett. **104**, 252301 (2010), arXiv:1002.1077
[6] G. Aad et al. (ATLAS Collaboration), Phys. Rev. Lett. **105**, 252303 (2010), arXiv:1011.6182
[7] K. Aamodt et al. (ALICE Collaboration), Phys.Lett. **B696**, 30 (2011), arXiv:1012.1004
[8] S. Chatrchyan et al. (CMS Collaboration), Phys.Rev. **C84**, 024906 (2011), arXiv:1102.1957
[9] M.H. Thoma, Phys. Lett. **B273**, 128 (1991)
[10] M.G. Mustafa, M.H. Thoma, Acta Phys. Hung. **A22**, 93 (2005), hep-ph/0311168
[11] M. Gyulassy, X.n. Wang, Nucl. Phys. **B420**, 583 (1994), nucl-th/9306003
[12] R. Baier, Y.L. Dokshitzer, A.H. Mueller, S. Peigne, D. Schiff, Nucl. Phys. **B483**, 291 (1997), hep-ph/9607355
[13] R. Baier, D. Schiff, B.G. Zakharov, Ann. Rev. Nucl. Part. Sci. **50**, 37 (2000), hep-ph/0002198
[14] M. Gyulassy, I. Vitev, X.N. Wang, B.W. Zhang (2003), nucl-th/0302077
[15] D. d'Enterria (2009), arXiv:0902.2011
[16] U.A. Wiedemann (2009), arXiv:0908.2306
[17] A. Majumder, M. van Leeuwen, Prog.Part.Nucl.Phys. **A66**, 41 (2011), arXiv:1002.2206
[18] S.A. Bass et al., Phys. Rev. **C79**, 024901 (2009), arXiv:0808.0908
[19] A. Adare et al. (PHENIX), Phys. Rev. Lett. **101**, 232301 (2008), arXiv:0801.4020
[20] A. Adare et al. (PHENIX), Phys. Rev. **C77**, 064907 (2008), arXiv:0801.1665
[21] J.C. Collins, D.E. Soper, G.F. Sterman, Nucl. Phys. **B261**, 104 (1985)
[22] J. Pumplin et al., JHEP **07**, 012 (2002), hep-ph/0201195
[23] A.D. Martin, R.G. Roberts, W.J. Stirling, R.S. Thorne, Eur. Phys. J. **C35**, 325 (2004), hep-ph/0308087
[24] M. Hirai, S. Kumano, T.H. Nagai, Phys. Rev. **C76**, 065207 (2007), arXiv:0709.3038
[25] D. de Florian, R. Sassot, M. Stratmann, Phys. Rev. **D76**, 074033 (2007), 0707.1506
[26] S. Albino, B.A. Kniehl, G. Kramer, Nucl. Phys. **B803**, 42 (2008), arXiv:0803.2768
[27] S.S. Adler et al. (PHENIX), Phys. Rev. Lett. **94**, 232301 (2005), nucl-ex/0503003
[28] K.J. Eskola, H. Paukkunen, C.A. Salgado, JHEP **04**, 065 (2009), arXiv:0902.4154
[29] F. Arleo, JHEP **0609**, 015 (2006), hep-ph/0601075
[30] Y. Mehtar-Tani, C.A. Salgado, K. Tywoniuk, Phys. Rev. Lett. **106**, 122002 (2011), arXiv:1009.2965
[31] Y. Mehtar-Tani, C. Salgado, K. Tywoniuk, Phys.Lett. **B707**, 156 (2012), arXiv:1102.4317
[32] Y. Mehtar-Tani, K. Tywoniuk (2011), arXiv:1105.1346
[33] J. Casalderrey-Solana, E. Iancu, JHEP **1108**, 015 (2011), arXiv:1105.1760

[34] R. Baier, Y.L. Dokshitzer, A.H. Mueller, S. Peigne, D. Schiff, Nucl. Phys. **B484**, 265 (1997), hep-ph/9608322

[35] R. Baier, Y.L. Dokshitzer, A.H. Mueller, D. Schiff, Nucl. Phys. **B531**, 403 (1998), hep-ph/9804212

[36] B.G. Zakharov, JETP Lett. **63**, 952 (1996), hep-ph/9607440

[37] B.G. Zakharov, JETP Lett. **65**, 615 (1997), hep-ph/9704255

[38] U.A. Wiedemann, Nucl. Phys. **B588**, 303 (2000), hep-ph/0005129

[39] C.A. Salgado, U.A. Wiedemann, Phys. Rev. **D68**, 014008 (2003), hep-ph/0302184

[40] N. Armesto, C.A. Salgado, U.A. Wiedemann, Phys. Rev. **D69**, 114003 (2004), hep-ph/0312106

[41] M. Gyulassy, P. Levai, I. Vitev, Nucl. Phys. **B571**, 197 (2000), hep-ph/9907461

[42] M. Gyulassy, P. Levai, I. Vitev, Nucl. Phys. **B594**, 371 (2001), nucl-th/0006010

[43] M. Gyulassy, P. Levai, I. Vitev, Phys. Lett. **B538**, 282 (2002), nucl-th/0112071

[44] S. Wicks (2008), arXiv:0804.4704

[45] P.B. Arnold, Phys. Rev. **D80**, 025004 (2009), arXiv:0903.1081

[46] M. Djordjevic, M. Gyulassy, Nucl. Phys. **A733**, 265 (2004), nucl-th/0310076

[47] S. Wicks, W. Horowitz, M. Djordjevic, M. Gyulassy, Nucl. Phys. **A784**, 426 (2007), nucl-th/0512076

[48] M. Djordjevic, U.W. Heinz, Phys. Rev. Lett. **101**, 022302 (2008), arXiv:0802.1230

[49] X.N. Wang, X.f. Guo, Nucl. Phys. **A696**, 788 (2001), hep-ph/0102230

[50] A. Majumder (2009), 0901.4516

[51] P.B. Arnold, G.D. Moore, L.G. Yaffe, JHEP **12**, 009 (2001), hep-ph/0111107

[52] P.B. Arnold, G.D. Moore, L.G. Yaffe, JHEP **06**, 030 (2002), hep-ph/0204343

[53] U.A. Wiedemann, Nucl. Phys. **A690**, 731 (2001), hep-ph/0008241

[54] W.A. Horowitz, B.A. Cole, Phys. Rev. **C81**, 024909 (2010), arXiv:0910.1823

[55] S. Wicks (2008), Ph.D thesis Columbia University, http://proquest.umi.com/pqdweb?sid=1&Fmt=2&clientId=79356&RQT=309&VName=PQD&did=1614268891

[56] S. Caron-Huot, C. Gale, Phys.Rev. **C82**, 064902 (2010), 1006.2379

[57] P. Arnold, Phys. Rev. **D79**, 065025 (2009), arXiv:0808.2767

[58] Http://csalgado.web.cern.ch/csalgado/swqw.html

[59] N. Armesto, L. Cunqueiro, C.A. Salgado, W.C. Xiang, JHEP **02**, 048 (2008), arXiv:0710.3073

[60] K. Zapp, G. Ingelman, J. Rathsman, J. Stachel, U.A. Wiedemann, Eur. Phys. J. **C60**, 617 (2009), arXiv:0804.3568

[61] K. Zapp, J. Stachel, U.A. Wiedemann, Phys. Rev. Lett. **103**, 152302 (2009), arXiv:0812.3888

[62] N. Armesto, L. Cunqueiro, C.A. Salgado, Eur. Phys. J. **C63**, 679 (2009), arXiv:0907.1014

[63] N. Armesto, G. Corcella, L. Cunqueiro, C.A. Salgado, JHEP **11**, 122 (2009), arXiv:0909.5118

[64] M. Djordjevic, Phys. Rev. **C80**, 064909 (2009), arXiv:0903.4591

[65] P.B. Arnold, G.D. Moore, L.G. Yaffe, JHEP **11**, 057 (2001), hep-ph/0109064

[66] S. Jeon, G.D. Moore, Phys. Rev. **C71**, 034901 (2005), hep-ph/0309332

[67] E. Braaten, R.D. Pisarski, Phys. Rev. Lett. **64**, 1338 (1990)

[68] E. Braaten, R.D. Pisarski, Nucl. Phys. **B337**, 569 (1990)

[69] G.Y. Qin et al., Phys. Rev. Lett. **100**, 072301 (2008), arXiv:0710.0605

[70] B. Schenke, C. Gale, G.Y. Qin, Phys. Rev. **C79**, 054908 (2009), arXiv:0901.3498

[71] P. Aurenche, B. Zakharov, JETP Lett. **85**, 149 (2007), hep-ph/0612343

[72] P. Aurenche, F. Gelis, H. Zaraket, JHEP **05**, 043 (2002), hep-ph/0204146

[73] S. Caron-Huot, Phys. Rev. **D79**, 065039 (2009), arXiv:0811.1603

[74] J.w. Qiu, G.F. Sterman, Nucl. Phys. **B353**, 137 (1991)

[75] J.w. Qiu, G.F. Sterman, Nucl. Phys. **B353**, 105 (1991)

[76] X.f. Guo, X.N. Wang, Phys. Rev. Lett. **85**, 3591 (2000), hep-ph/0005044

[77] A. Majumder, Phys.Rev. **D85**, 014023 (2012), 0912.2987

[78] B.A. Kniehl, G. Kramer, B. Potter, Nucl. Phys. **B582**, 514 (2000), hep-ph/0010289

[79] J. Adams et al. (STAR), Phys. Lett. **B637**, 161 (2006), nucl-ex/0601033

[80] J. Adams et al. (STAR), Phys. Rev. Lett. **91**, 172302 (2003), nucl-ex/0305015

[81] S.S. Adler et al. (PHENIX), Phys. Rev. Lett. **91**, 072301 (2003), nucl-ex/0304022

[82] S.S. Adler et al. (PHENIX), Phys. Rev. **C69**, 034910 (2004), nucl-ex/0308006

[83] P.B. Arnold, W. Xiao, Phys. Rev. **D78**, 125008 (2008), arXiv:0810.1026

[84] We note that the ASW–SH implementation [39] is only in terms of the Poisson convoluted energy loss probability distribution, which we will discuss in detail further below. The comparison shown here was obtained from an independent numerical implementation of the massless ASW–SH formula that well reproduces the Poisson convolution results of [39].

[85] In general one needs to consider the distribution in differences in distance between successive scattering centers. However at first order in opacity there is only one scattering center; as one may always set the initial value of z to 0, $\rho(z)$ is the absolute distance to the first scattering center.

Appendix A: Common definition of medium properties $\hat{q}$, μ and λ

In this Appendix we review a number of commonly used equations to relate properties of the medium, such as the transport coeffient $\hat{q}$, mean free path λ and temperature T.

1. The basis: a HTL plasma

The basis for all the equations used are free scattering cross sections, supplemented with elements of Hard

Thermal Loop (HTL) field theory to screen the soft divergence in the free cross section.

For a medium with temperature T, the Debye screening mass m_D is

$$m_D^2 = (1 + \frac{1}{6}N_f)g^2T^2, \tag{A1}$$

where g is the coupling constant ($g^2 = 4\pi\alpha_S$) and N_f is the number of quark flavours (0 for a pure gluon gas).

We also define a number density of the medium $\mathcal{N}$ [83]:

$$\mathcal{N} = \frac{\zeta(3)}{\zeta(2)}(1 + \frac{1}{4}N_f)T^3. \tag{A2}$$

The differential scattering rate for a hard parton traversing the medium is known for two limits of the exchanged momentum $q_\perp$ [83]:

$$\frac{d\Gamma_{el}}{d^2q_\perp} \simeq \frac{C_R}{(2\pi)^2} \times \begin{cases} \frac{g^2Tm_D^2}{\mathbf{q}_\perp^2(\mathbf{q}_\perp^2+m_D^2)} & \text{if } |\mathbf{q}_\perp| \ll T \\ \frac{g^4\mathcal{N}}{\mathbf{q}_\perp^4} & \text{if } |\mathbf{q}_\perp| \gg T, \end{cases} \tag{A3}$$

the relevant color factor C_R for most energy loss calculations is the color factor of the gluon $C_R = C_A = 3$.

2. Transport coefficient $\hat{q}$

The transport coefficient $\hat{q}$, which is the only medium parameter that enters in the multiple soft scattering approximation, is defined as the mean momentum kick squared per unit path length

$$\hat{q} = \rho \int d^2q_T\, q_T^2\, \frac{d\sigma}{d^2q_T} \equiv \int_0^{q_{\max}} d^2q_\perp \frac{d\Gamma_{el}}{d^2q_\perp}\mathbf{q}_\perp^2, \tag{A4}$$

in which Γ_{el} is the rate for elastic collisions in the plasma, $\mathbf{q}_\perp$ is the transverse momentum exchanged with the medium $q_{\max}$ is the upper limit for the exchanged momentum, which represents an ultraviolet cut-off.

The transport coefficient $\hat{q}$ integrates over all momentum transfers $\hat{q}$ and can therefore in general not be based on only the low or the high $q_\perp$ limit given in Eq. A3. The following expression provides a smooth interpolation between the two limits

$$\frac{d\Gamma_{el}}{d^2q_\perp} \simeq \frac{C_R}{(2\pi)^2} \times \frac{g^4\mathcal{N}}{\mathbf{q}_\perp^2(\mathbf{q}_\perp^2 + m_D^2)}. \tag{A5}$$

This interpolation is illustrated in Fig. 24 which shows low energy limit of Eq. (A3) (curve labeled *Soft*) together with Eq. A5 (curve labeled *Interpolated*). In the soft region the interpolated curve deviates by 17% due to the difference in the numerator and approaches the high energy limit smoothly at large $q_\perp$.

The resulting transport coefficient is

$$\hat{q}(T) = \frac{C_R g^4 \mathcal{N}(T)}{4\pi} \ln\left(\frac{q_{\max}^2(T)}{m_D^2(T)} + 1\right). \tag{A6}$$

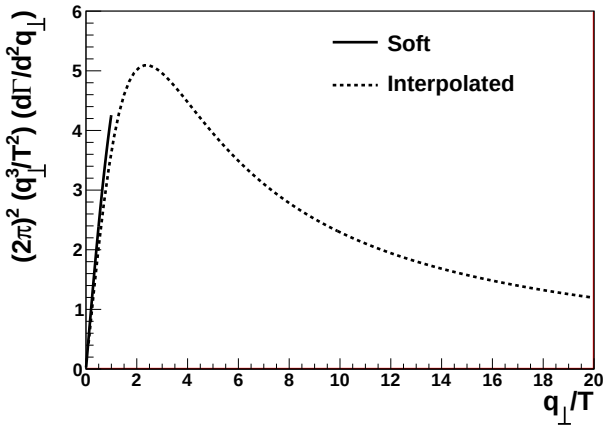


FIG. 24: Differential elastic cross-section as function of $q_\perp$ for the different energy limits. The curves labeled with *Interpolated* correspond to the expression given in Eq. (A5). Curves labeled with *Soft* correspond to the low energy limit in Eq. (A3).

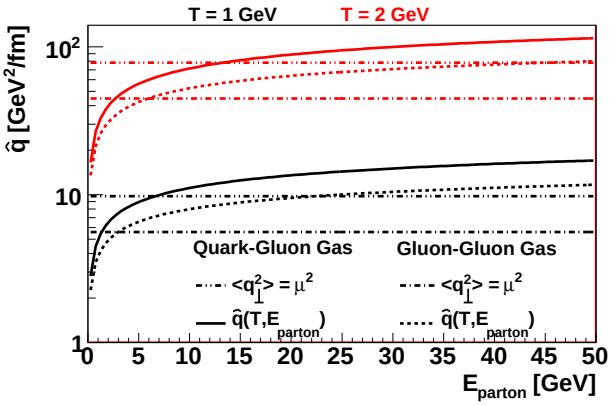


FIG. 25: The transport coefficient as function of the energy of the parton traversing a medium of different tempertures. The transport coefficient is calculated in the hard thermal loop formalism as in equation A6.

In the high energy limit the constant in the argument of the logarithm vanishes but in the low energy limit its presence is crucial because otherwise unphysical negative values for $\hat{q}$ are possible. In a realistic medium created in a heavy-ion collision naturally both cases will be present.

The value for $q_{\max}$ is expected to fall in the hard scattering regime, where the scattering centers can be approximated as static, leading to $q_{\max} = g(ET^3)^{1/4}$ as has been argued in [73]. The dependence of $q_{\max}$ on the energy of the incoming parton E leads to a logarithmic dependence of $\hat{q}$ on E. Figure 25 compares the resulting energy-dependent $\hat{q}$ to a commonly used energy-independent expression for $\hat{q}$

$$\hat{q} = \frac{\langle q_\perp^2 \rangle}{\lambda} \approx \frac{m_D^2}{\lambda}, \tag{A7}$$

where it is assumed that the mean squared momentum exchange per scattering is equal to m_D^2 and the mean free path λ is calculated as given below.

3. Mean free path

The mean free path λ used in the opacity expansion is usually calculated based on a Quark Gluon Plasma with static scattering centers, using the scattering rate

$$\frac{d\Gamma_{el}}{d^2q_\perp} \simeq \frac{C_R}{(2\pi)^2} \times \frac{g^4\mathcal{N}}{(\mathbf{q}_\perp^2 + m_D^2)^2}, \tag{A8}$$

which is very similar to Eq. A5, except for a change in the denominator which is needed to obtain a finite result for λ.

This leads to the following expression for the number of scattering centers

$$\frac{L}{\lambda} = L \int d^2q_\perp \frac{d\Gamma_{el}}{d^2q_\perp} = 4\pi C_R \mathcal{N} \frac{\alpha_s^2}{m_D^2} L. \tag{A9}$$